university of groningen / faculty of science and engineering

July 19, 2024

Quantification of backgrounds in the high-q^2 region of $R(\Lambda)$

Master Research Project (23/24)

Author:
Sander Bouma (S3772721)

Supervisor:
Mick Mulder

Abstract

This analysis aims to investigate the background modes present in the measurement of $R(\Lambda)$ in the high-q^2 region. This is the ratio of $\mathcal{B}(\Lambda_b^0 \to \Lambda^0 \mu^+ \mu^-)$ and $\mathcal{B}(\Lambda_b^0 \to \Lambda^0 e^+ e^-)$ in the region of $14.3\ \text{GeV}^2/c^4 < q^2 < 20.0\ \text{GeV}^2/c^4$, where q^2 is the invariant mass of the dilepton pair of the decay. The $R(\Lambda)$ analysis uses the Run 1 and Run 2 LHCb datasets and aims to test Lepton Flavour Universality as well as performing the first measurement of the $\Lambda_b^0 \to \Lambda^0 e^+ e^-$branching fraction. $R(\Lambda)$ suffers from low statistics; therefore, it is vital to know which backgrounds are present in the data, how much they contribute and how they can be modeled. In this analysis, the backgrounds in both the muon and electron modes are investigated. An estimation of the yields of each background is made from efficiencies (from MC data) and branching fractions to determine which backgrounds are most likely to be significant. A study of the combinatorial background is not performed here, as it is a separate study on its own. It was estimated that the $\Lambda_b^0 \to \Lambda_c^+ (\to \Lambda^0 \ell^+ \nu_\ell) \ell^- \overline{\nu}_\ell$ decay has the highest background yield, but by employing an Λ_c^+-veto on the data it was shown that there was no significant contribution in the high-q^2 region. The contribution of the $B^0 \to K_S^0 (\to \pi^+ \pi^-) \ell^+ \ell^-$ background was shown to be in agreement with its expectation; a yield of around 2.0% relative to the signal yield. Further research should investigate the contribution of partially reconstructed backgrounds, perform studies on the effectiveness of a K_S^0 veto and the q^2_{track} cut in the electron mode, and model the double hadron misID background.

Contents

1 Introduction

The Standard Model (SM) of particle physics has been successful in providing an understanding of the fundamental particles and their interactions which govern our Universe. From the elegant symmetry of gauge theories to the spontaneous breaking of electroweak symmetry [1, 2, 3], the Standard Model has demonstrated remarkable predictive power, accurately describing the behavior of particles and their interactions across a wide range of energies. Its predictions have been confirmed with remarkable precision through experiments conducted worldwide. Examples include the measurements of the $W^{\pm}$ and Z^0 bosons [4] and the discovery of the Higgs boson [5].

Despite its successes, there are still open questions that the Standard Model is unable to provide an answer for. It does not explain the abundance of matter over anti-matter in our Universe [6], the observation of dark matter [7] and it does not provide a theory of (quantum) gravity. Because of these unanswered questions, physicists worldwide are looking to extend the Standard Model with Beyond the Standard Model (BSM) theories, which aim to provide an answer to some of these mysteries. One way to test the Standard Model and look for physics beyond it is by testing Lepton Flavour Universality (LFU). This is the notion that (according to the Standard Model) the weak interaction should treat different flavours of leptons (electrons, muons, taus) in an identical manner. Deviations from Lepton Flavour Universality could signal the presence of new (BSM) physics which could provide possible solutions to these unsolved mysteries.

Lepton Flavour Universality tests typically involve the measurement of specific decay processes into different lepton flavours. Examples include decays such as $B^+ \to K^+\ell^+\ell^-$ or $B^0 \to K^{*0}\ell^+\ell^-$, where $\ell^+\ell^-$ is a lepton pair of flavour ℓ [8]. The ratio of branching fractions of the muonic decay with respect to the electronic decay is then used to test Lepton Flavour Universality. According to the Standard Model, this ratio (denoted R) is approximately equal to unity, because muons and electrons are treated equally and should therefore be produced at the same rate (aside from corrections arising due to their mass differences). If this ratio deviates, it could be a sign that different lepton flavours are not treated equally, as some Beyond Standard Model theories predict [9, 10].

The research in this thesis is on testing Lepton Flavour Universality in $\Lambda_b^0 \to \Lambda^0\ell^+\ell^-$ decays, where the leptons are either muons or electrons. This is the first analysis testing Lepton Flavour Universality using baryonic decays with a resonant hadronic final state particle (the Λ^0 baryon). This thesis aims to quantify and provide a better understanding of the backgrounds that are present in these Λ_b^0 decays, as a precise understanding of the background events can help distinguish them from our signal events and thus help in constraining the result for $R(\Lambda)$. Since $R(\Lambda)$ is a ratio of signal yields of the muonic and electronic decay modes, any background that is incorrectly accounted as signal directly affects the result of this ratio. The main research goal of this thesis is:

How much do the different backgrounds contribute to $R(\Lambda)$ in the high-q^2 region?

The amount of background expected in data is estimated, based on the branching fraction, production rate, and relative efficiency compared to signal. Two of these backgrounds are further explored by data-driven methods and an outlook is given for future studies to determine the abundance of other backgrounds.

2 Theory

2.1 The Standard Model of particle physics

Our current understanding of the fundamental particles and their interactions is described by the Standard Model (SM) of particle physics. The SM is a theoretical framework that describes the elementary particles that make up matter and three of the four fundamental forces (electromagnetic, weak and strong) through which they interact. The particles that make up matter are known as fermions. These include quarks (which combine to form hadrons) and leptons (such as electrons and neutrinos). The forces through which these fermions interact are mediated through gauge bosons. The electromagnetic force, described by Quantum Electrodynamics, is mediated by photons, the weak force is mediated by $W^{\pm}$ and Z^0 bosons and the strong force, described by Quantum Chromodynamics, is mediated by gluons. All of these interactions are described by the gauge group $\mathrm{SU}(3)_C \otimes \mathrm{SU}(2)_L \otimes \mathrm{SU}(1)_Y$. This group encapsulates the symmetries that define the interactions in the Standard Model. Each part of this group corresponds to one of the three fundamental forces (excluding gravity). The latest addition to the SM is the Higgs boson, which was discovered in 2012 [5]. This scalar boson is the result of the breaking of the gauge symmetry, which gives masses to the $W^{\pm}$ and Z^0 bosons while leaving the photon massless [11].

The elementary particles are organized into three generations, or families, which are sets of particles with similar properties but differing masses. Each generation consists of two types of quarks and two types of leptons (one charged lepton and one neutrino). Particles in higher generations are more massive and less stable, typically decaying into particles of lower generations. A summary of the elementary particles of the SM and their properties is shown in Figure 1.

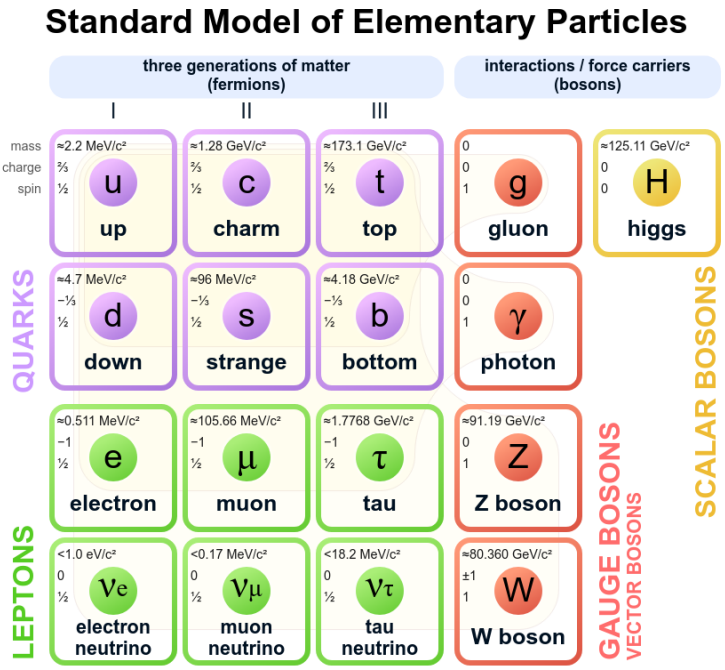

Figure 1: Schematic overview of the elementary particles and their properties in the Standard Model of particle physics [12].

2.2 Flavour changing interactions

The six different types of quarks and six different types of leptons are known as flavours. In the SM, quark and lepton flavours can change through interactions mediated by the weak force. This force is unique in its ability to change one type of quark or lepton into another type. These flavour changing interactions are described by the Cabibbo-Kobayashi-Maskawa (CKM) matrix [13, 14]:

$$\begin{pmatrix} d' \\ s' \\ b' \end{pmatrix} = \begin{pmatrix} V_{ud} & V_{us} & V_{ub} \\ V_{cd} & V_{cs} & V_{cb} \\ V_{td} & V_{ts} & V_{tb} \end{pmatrix} \begin{pmatrix} d \\ s \\ b \end{pmatrix}. \tag{1}$$

The CKM matrix is a unitary matrix that relates the mass eigenstates of quarks (the states with definite mass) to their weak eigenstates (the states that participate in weak interactions). The CKM matrix elements V_{ij} describe the strength of the transition from an up-type quark i to a down-type quark j. These flavour changing interactions are mediated by $W^{\pm}$ bosons and can occur through Flavour Changing Charged Currents and Flavour Changing Neutral Currents.

Flavour Changing Charged Currents (FCCCs) involve interactions where a quark changes flavour and the type is also changed. Flavour Changing Neutral Currents (FCNCs) involve interactions where a quark changes flavour without a change in type. According to the SM, FCNC interactions can only occur at loop level and are forbidden at tree-level. This makes FCNC interactions suppressed, meaning they are orders of magnitude less abundant compared to FCCC interactions. Lowest order Feynman diagrams of these flavour changing currents are shown in Figure 2a (FCCC) and 2b (FCNC).

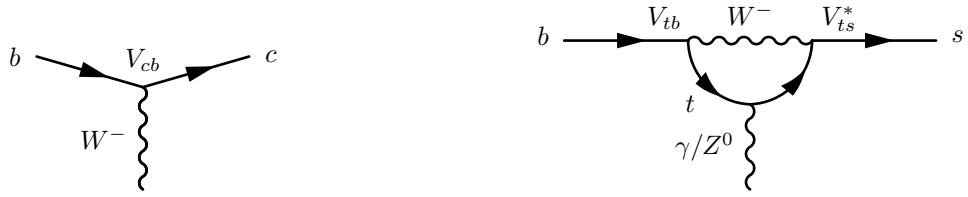

(a) FCCC interaction (b) FCNC interaction

Figure 2: Lowest order Feynman diagram of an FCCC interaction (a) and an FCNC interaction (b).

2.3 Lepton Flavour Universality and $b \to s\ell^+\ell^-$ transitions

FCNCs, such as $b \to s\ell^+\ell^-$ transitions, are particularly interesting in the search for New Physics (NP) beyond the SM because they are highly suppressed processes in the SM. This suppression makes them sensitive to potential contributions from new particles or interactions that are not accounted for in the SM. Examples of these BSM theories include theories involving Z' particles [10] or leptoquarks [9]. These hypothetical particles can have tree-level contributions in $b \to s\ell^+\ell^-$ transitions, therefore any significant deviations from SM predictions could indicate the presence of NP beyond the SM. Tree-level Feynman diagrams for these interactions, as well as the SM loop diagram are shown in Figure 3.

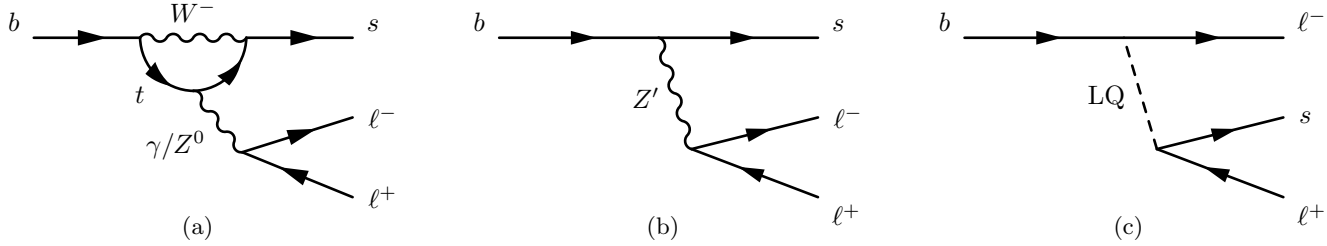

(a) (b) (c)

Figure 3: Lowest order Feynman diagrams of a $b \to s\ell^+\ell^-$ transition as predicted by the SM (a), and as predicted by theories involving Z'-bosons (b) or leptoquarks (c).

One way to probe these $b \to s\ell^+\ell^-$ transitions and look for new physics is by testing Lepton Flavour Universality (LFU). This is the property of the SM that all leptons share the same interactions and have the same coupling

strengths to gauge bosons, independent of their flavour. It is an interesting property to test because LFU can be broken in many NP scenarios. BSM interactions involving Z' bosons or leptoquarks could potentially have a larger coupling to muons than electrons, which would therefore violate LFU.

Numerous analyses involving $b \to s\ell^+\ell^-$ transitions have been performed and so far no clear violation of LFU has been found. These analyses test LFU through the observable R, which is defined as the ratio of branching fractions, integrated over a certain q^2 range:

$$R \equiv \frac{\int_{q^2_{\min}}^{q^2_{\max}} \frac{\mathcal{B}(H_b \to H_s \mu^+\mu^-)}{\mathrm{d}q^2} \mathrm{d}q^2}{\int_{q^2_{\min}}^{q^2_{\max}} \frac{\mathcal{B}(H_b \to H_s e^+e^-)}{\mathrm{d}q^2} \mathrm{d}q^2}, \tag{2}$$

where H_b and H_s are hadrons containing a b or an s quark respectively, and q^2 is the invariant mass squared of the leptons. This is defined as:

$$q^2 \equiv (\mathbf{p}_{\ell^+} + \mathbf{p}_{\ell^-})^2, \tag{3}$$

where $\mathbf{p}_{\ell^+}$ and $\mathbf{p}_{\ell^-}$ are the four-momenta of the leptons. To date, the LHCb collaboration has measured the ratios of R_K and $R_{K^{*0}}$ [8], R_{pK} [15] and $R_{K^0_S}$ and $R_{K^{*+}}$ [16], where the asterisk denotes an excited state. These ratios are treated together, as the decays are the same aside for the presence of an up-quark ($K^\pm$) or down-quark (K^0). Some of these ratios had shown some tension with their SM predictions, due to previously underestimated hadronic backgrounds, but the most recent measurements of $R_{K^0_S}$ and $R_{K^{*+}}$ are consistent with SM predictions. An overview of these results is shown in Figure 4.

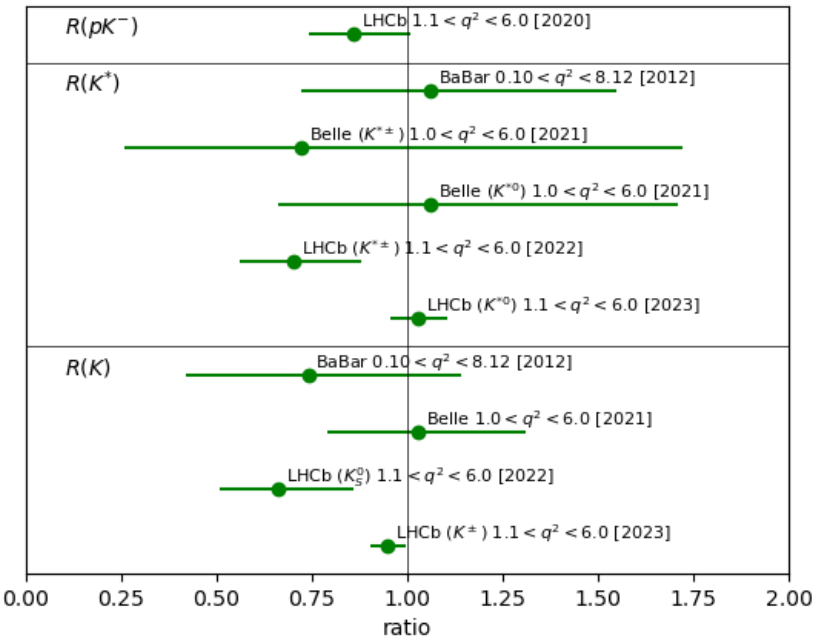

Figure 4: Summary of lepton flavour universality tests performed using rare b-hadron decays in various q^2 ranges [17]. The SM prediction for these ratios is about 1.00 ± 0.01 (or better).

To date, no measurement of $R(\Lambda)$ has been performed. The decay mode of interest for $R(\Lambda)$ is $\Lambda_b^0 \to \Lambda^0(\to p\pi^-)\ell^+\ell^-$, where the Λ^0 decays into a proton and a pion and $\ell^+\ell^-$ are either muons or electrons. This decay is kinematically interesting as it involves a $b \to s\ell^+\ell^-$ transition in baryons as opposed to mesons and $R(\Lambda)$ explores a higher (unexplored) q^2 region compared to other analysis. On top of that, the Λ_b^0 baryon can be produced polarised and is stable under strong interactions, allowing for precise form factor calculations [18]. Studying this decay can give more insight into the underlying Wilson Coefficients, specifically C_9 and C_{10} [19]. Probing LFU in $R(\Lambda)$ could provide more insight in any BSM contributions that could be hiding in these coefficients.

3 The LHC and the LHCb experiment

The data used for the measurement of $R(\Lambda)$ is collected at the LHCb detector at CERN. The LHCb detector is one of the four detectors along the Large Hadron Collider (LHC), located near Geneva. In the LHC, proton beams are accelerated in opposite directions and made to collide at a centre-of-mass energy ($\sqrt{s}$) of 7 TeV in 2011, 8 TeV in 2012 and 13 TeV between 2015 and 2018. These data-taking periods are also known as runs, which are summarized in Table 1. The data is taken with the magnetic field in the detector pointing upwards (MU) or downwards (MD).

Run	Year	$\sqrt{s}$	Magnet polarity	Integrated luminosity [pb^{-1}]
R1	2011	7 TeV	MU	475.31
			MD	592.94
	2012	8 TeV	MU	996.20
			MD	987.52
R2p1	2015	13 TeV	MU	122.23
			MD	162.37
	2016	13 TeV	MU	777.71
			MD	842.21
R2p2	2017	13 TeV	MU	818.38
			MD	862.09
	2018	13 TeV	MU	1107.48
			MD	1024.40

Table 1: Summary of the data-taking periods of the LHCb detector, with the centre-of-mass energy and the amount of data collected specified.

3.1 The LHCb detector

The aim of the LHCb experiment is to study CP violation and other rare phenomena in b-hadron decays with high precision. In order to achieve this, the LHCb detector is designed as a forward spectrometer of conical shape. This forward geometry optimizes the detection of b-hadrons produced in proton-proton (pp) collisions. Over its various runs, the LHCb detector has undergone several upgrades and improvements. These upgrades have improved the different subdetector systems as well as improve the capability to handle the increase in luminosity.

Each subdetector system is designed to perform specific tasks necessary for the detection and analysis of particles resulting from pp collisions. These subdetector systems aim to reconstruct the location of decay vertices, the types of particles resulting from these decays and the four-momenta of the final-state particles. Using this information, complete decay processes can be reconstructed and their parameters can be measured and compared to SM predictions. A schematic of the full LHCb detector and its subdetector systems is shown in Figure 5.

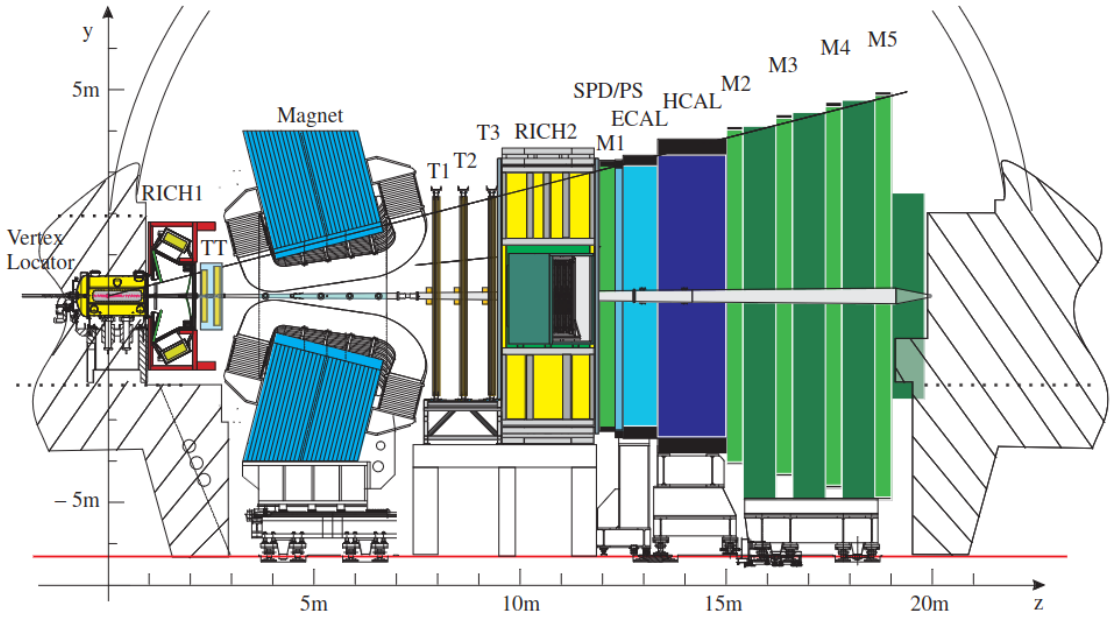

Figure 5: Schematic of the LHCb detector and its subdetector systems as per Run 1 and Run 2 [20].

3.1.1 Particle tracking

The subdetector closest to the interaction point is the Vertex Locator (VELO). The aim of this subdetector is to reconstruct decay vertices of short-lived particles, and find their displacement to the primary vertex. The VELO achieves this by reconstructing tracks based on hits from charged particles in silicon strips. These strips are placed on 21 semi-circular silicon sensor modules which are placed along the z-axis. These modules measure the r (radial distance) or ϕ (azimuthal angle) coordinates of these hits in the plane orthogonal to the z-axis. Consecutive hits in these modules are combined to reconstruct the tracks of the charged particles. These tracks can then be extrapolated to find vertices from which these particles originate.

Not all particles decay inside the VELO. Particles that decay outside of the VELO are tracked by the rest of the tracking system. The tracking system consists of the VELO and a dipole magnet together with different tracking stations (TT, T1, T2 and T3). These tracking stations use silicon strips to measure hits of charged particles passing through them. Particles leave hits in the TT, after which charged particles are then bent in the magnetic field. They then pass through tracking stations T1-T3, leaving more position measurements. From these measurements, a track is reconstructed and the sign of the particle's charge as well as its momentum can then be determined.

Tracking information from the T-stations and the VELO can be combined to get a higher resolution on the particle's momentum. However, it is not always possible to match tracks from the T-stations to tracks from the VELO (or other T-stations). The possibilities of such combined tracks are schematically shown in Figure 6.

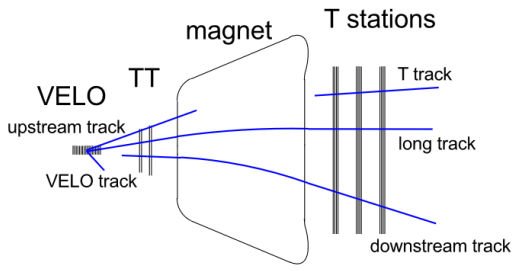

Figure 6: Different track reconstruction options based on whether the particle left hits in the VELO, the upstream TT-station and/or the downstream T-stations [21].

When a Λ_b^0 baryon decays, it has an average decay length of the order of a cm and therefore decays inside the VELO. The resultant Λ^0 baryon can decay either inside or outside the VELO, due to its decay length of the order of a meter. This produces a proton and a pion. Depending on the decay location of the Λ^0, these secondary particles (proton and pion) can have different trajectories. When the decay took place inside the VELO, the proton and pion can leave hits there. They then travel through the TT-station, the magnetic field and the T-stations, resulting in two long tracks (referred to as LL). Alternatively, when the Λ^0 decays outside of the VELO, the proton and pion only leave hits in the TT-station and the T-stations (and not in the VELO), resulting in two downstream tracks (referred to as DD). The data of the $R(\Lambda)$ analysis is split up into these two categories.

3.1.2 Particle identification

Just the reconstruction of a particle's trajectory and momentum is insufficient to fully identify the the type of particle that traversed the detector. Particle identification (PID) is provided by four different detector systems: the calorimeter systems, the two RICH detectors and the muon stations.

The calorimeter system consists of the electromagnetic calorimeter (ECAL) and the hadronic calorimeter (HCAL). These are made up of scintillating material interspersed with layers of dense material, which is chosen to have a high electromagnetic or hadronic cross-section. When a particle interacts with this dense material, a cascade of secondary particles is created. These secondary particles pass through the scintillating material, emitting light, which is then detected by photodetectors. The amount of light produced is proportional to the energy of the original particle. The ECAL is optimised for measuring electrons and photons, while the HCAL measures the energy of hadrons. Different particles leave different energy depositions in the ECAL and HCAL and can thereby be identified. Muons typically pass through the ECAL and HCAL with minimal energy loss. They are measured by the muon stations (M1-M5).

The Two Ring Imaging Cherenkov (RICH) detectors are placed between the different trackers. The primary role of these sub-detectors is the identification of charged hadrons, but they also aid in the identification of muons and electrons. The working principle of these detectors is the Cherenkov effect. Cherenkov radiation is emitted when particles traverse the detector with a velocity faster than the phase velocity of light in the medium. The emitted Cherenkov radiation is then detected by photodetectors and the Cherenkov angle is reconstructed. This angle is directly proportional to the velocity of the particle that traversed the RICH-detector, and taking this angle together with the particle's momentum information from the tracking system can provide information on its identity (see Figure 7). This information is used in a log-likelihood fit to different mass hypotheses to determine the identity of the particle.

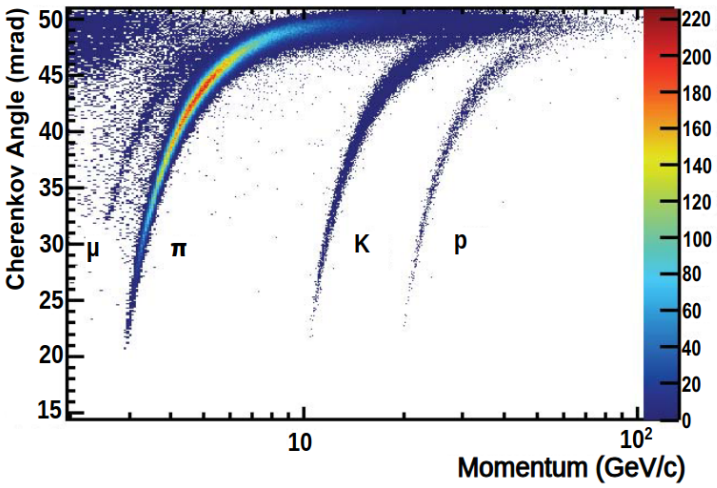

Figure 7: Reconstructed Cherenkov angle as a function of track momentum from RICH-1 measurements [22].

In Figure 7, it can be seen that for certain momentum ranges, the Cherenkov angles for different particles can overlap. This makes it possible to have mis-identifications of particles. A muon can for example be identified as a

pion and vice versa. The presence of these mis-identified particles in the data increases the background and can skew the $R(\Lambda)$ branching fraction ratio.

3.2 Data Flow

Due to the high collision rate at the LHCb, it is impossible to record all events that take place. To filter out the most interesting events, a trigger system is used. At the time of Run 1 and Run 2, the trigger system consisted of a low-level hardware trigger (L0) and two high-level software triggers (HLT1 and HLT2) [23]. The L0 trigger filters events by selecting events with high transverse momentum particles, which is indicative of interesting physics phenomena. HLT1 then partially reconstructs these events and makes a more refined selection based on well-reconstructed tracks and events that have a significant displacement from the primary vertex, indicative of long-lived b-hadrons. This data is then stored and passed on to HLT2. HLT2 reconstructs specific decays that analysts are interested in. HLT2 partially reconstructs the $\Lambda_b^0 \to \Lambda^0 \ell^+ \ell^-$ decay based on a selection of lepton and Λ^0 candidates and applies initial cuts based on the Λ_b^0 mass and vertex detachment variables .

The events that pass the trigger-line are then saved for offline reconstruction. This is a more thorough reconstruction than during the real-time processing of HLT1 and HLT2. This reconstruction includes the precise fitting of particle trajectories using hits measured by the detector, a detailed reconstruction of the primary and secondary decay vertices, an improved identification of particles and a more detailed calibration of energy deposits in the calorimeter system.

After reconstruction a stripping process takes place. This process involves applying additional selection criteria to the reconstructed events to create more refined datasets (called "stripping lines") that are specific to various physics analyses. The output of the stripping process is a set of smaller, more manageable datasets that contain events of interest for specific physics analyses. These events are stored in DST format, which contains event data including tracks, vertices and PID information. The DaVinci software is used to convert this to Ntuples, which are a type of multidimensional array where each column represents a different variable (such as momentum components, PID information and information on decay vertices), and each row represents an individual event. These Ntuples are then used for further analysis.

In addition, Monte Carlo (MC) simulations are used in parallel to real data processing to model the signal and background events that end up in the final selection. These simulated events are processed through a detailed detector simulation to model the detector response, and then undergo the same reconstruction and stripping process as the data. This MC data is used to better understand the behaviour of signal and background in our data, and allows us to perform efficiency calculations. The efficiency is a measure of the fraction of decays that make it through one (or more) step(s) in the measurement and data-flow process. A schematic of the entire data-flow process is shown in Figure 8.

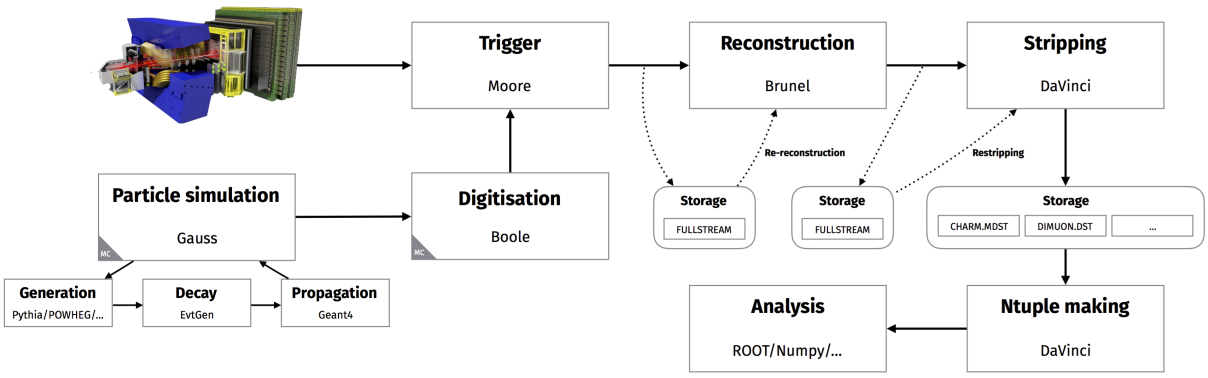

Figure 8: Schematic of the data-flow after measurement by the LHCb detector, and the specific software tools used for each step of the reconstruction [24].

In the final analysis, the Ntuples are used to measure $R(\Lambda)$. At this stage, analysis-specific selection criteria and cuts are applied to optimize signal purity and reduce background contamination. This procedure is described in more detail in the next section.

4 The R(Λ) analysis

For the determination of $R(\Lambda)$, the main region of interest is the high-q^2 region. In this region, the branching fraction of the rare $\Lambda_b^0 \to \Lambda^0 \ell^+ \ell^-$ decay is the largest. The high-q^2 region is the region where 14.3 GeV$^2/c^4 < q^2 < 20.0$ GeV$^2/c^4$, where the limit of 20.0 GeV$^2/c^4$ reflects the upper phase-space limit. The branching fraction of $\Lambda_b^0 \to \Lambda^0 \mu^+ \mu^-$ as a function of q^2 is shown in Figure 9. A similar branching fraction distribution is expected for the $\Lambda_b^0 \to \Lambda^0 e^+ e^-$ decay, as electrons and muons are treated equally in the SM.

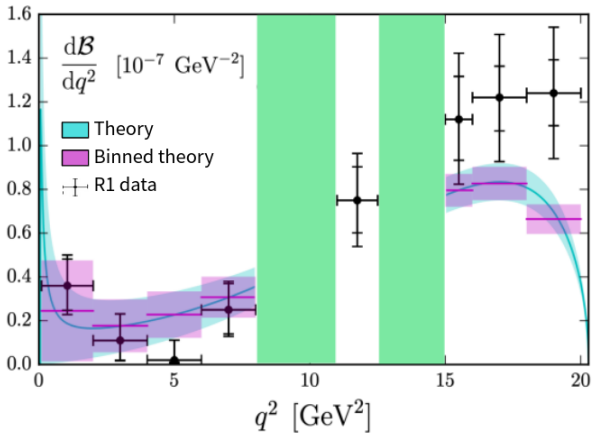

Figure 9: Branching fraction distribution of $\Lambda_b^0 \to \Lambda^0 \mu^+ \mu^-$ as a function of q^2, constructed from binned LHCb Run 1 data [25] and (binned) theory predictions [26]. The inner error bars represent the statistical and systematic uncertainty, whereas the the outer error bar includes the uncertainty of the $\mathcal{B}(\Lambda_b^0 \to \Lambda^0 J/\psi)$ normalisation. The green vertical bands show the excluded J/ψ and $\psi(2S)$ regions [27].

This division in q^2 is made to separate the rare $\Lambda_b^0 \to \Lambda^0 \ell^+ \ell^-$mode from the resonant $\Lambda_b^0 \to \Lambda^0 J/\psi (\to \ell^+ \ell^-)$ and $\Lambda_b^0 \to \Lambda^0 \psi(2S) (\to \ell^+ \ell^-)$ modes. J/ψ and $\psi(2S)$ are $c\bar{c}$-resonances with short lifespans that can rapidly decay into dilepton pairs, making these decays look similar to the rare mode when reconstructed by the detector. These resonances are therefore separated from the rare mode by dilepton invariant mass (q^2) constraints. The resonant J/ψ and $\psi(2S)$ modes are orders of magnitude more abundant than the non-resonant $\Lambda_b^0 \to \Lambda^0 \ell^+ \ell^-$ mode, as they occur at tree-level in the SM. The J/ψ and $\psi(2S)$ regions are used as cross-checks and as a normalisation channel. A q^2 region between the resonances is not considered as such a region would suffer from leakage from both J/ψ and $\psi(2S)$ regions, while simultaneously having too low statistics for the rare mode. The definitions of the different q^2 regions are presented in Table 2.

Muon mode		Electron mode	
q^2-region	Range	q^2-region	Range
Low-q^2	$0.1 < q^2 < 6.0$ GeV$^2/c^4$	Low-q^2	$0.1 < q^2 < 6.0$ GeV$^2/c^4$
J/ψ	$\lvert m(J/\psi) - \sqrt{q^2}\rvert < 50$ MeV$/c^2$	J/ψ	$6.0 < q^2 < 11.0$ GeV$^2/c^4$
$\psi(2S)$	$\lvert m(\psi(2S)) - \sqrt{q^2}\rvert < 50$ MeV$/c^2$	$\psi(2S)$	$11.0 < q^2 < 14.3$ GeV$^2/c^4$
High-q^2	$14.3 < q^2 < 20.0$ GeV$^2/c^4$	High-q^2	$14.3 < q^2_{\text{track}} < 20.0$ GeV$^2/c^4$

Table 2: Definitions of the q^2-regions of $R(\Lambda)$ for the muon and electron mode.

Aside from q^2-cuts, the $\Lambda_b^0 \to \Lambda^0 \mu^+ \mu^-$ (muon mode) data and the $\Lambda_b^0 \to \Lambda^0 e^+ e^-$ (electron mode) data are divided into different categories of data-taking periods (R1, R2p1 and R2p2) and proton-pion track types (DD and LL). The analysis is performed with the $\Lambda_b^0 \to \Lambda^0 e^+ e^-$ mode blinded, because the branching fraction of this decay has not been measured yet. This means that the data in the regions of q^2 and $m(\Lambda^0 e^+ e^-)$ (and similar quantities) where the signal is expected are not looked at before the analysis framework is finished and all cross-checks have been performed.

4.1 Bremsstrahlung losses in $\Lambda_b^0 \to \Lambda^0 e^+ e^-$

The most notable difference in the measurements of $\Lambda_b^0 \to \Lambda^0 e^+ e^-$ and $\Lambda_b^0 \to \Lambda^0 \mu^+ \mu^-$ comes from bremsstrahlung radiation, which is much more emitted from electrons than from muons as they pass through the LHCb detector. For electrons this effect is in the order of 10% on average, while for muons bremsstrahlung losses are negligible. This leads to vastly different momentum resolutions for the muon mode and the electron mode. This is also the reason the q^2-regions for the resonance mode can be defined tighter for the muon mode than for the electron mode.

To compensate for these bremsstrahlung losses, a bremsstrahlung recovery algorithm is implemented for electrons. This algorithm looks for compatible energy clusters in the ECAL and adds this energy back to the corresponding electrons. However, this recovery is imperfect as photons can still be missed or incorrectly assigned to electrons, in which case the electron momentum will be overestimated. This effect is also seen in the two-dimensional distributions in Figure 10, where the diagonal radiative tails arise due to missing lepton momentum. For electrons these radiative tails arise mainly due to bremsstrahlung losses. These tails are also present in the muon mode, where their main cause is final-state radiation, which is not reconstructed. In the electron mode (Figure 10b), the tails also extend to the upper mass side, indicating an overestimation of the electron momentum due to incorrectly assigned bremsstrahlung energy.

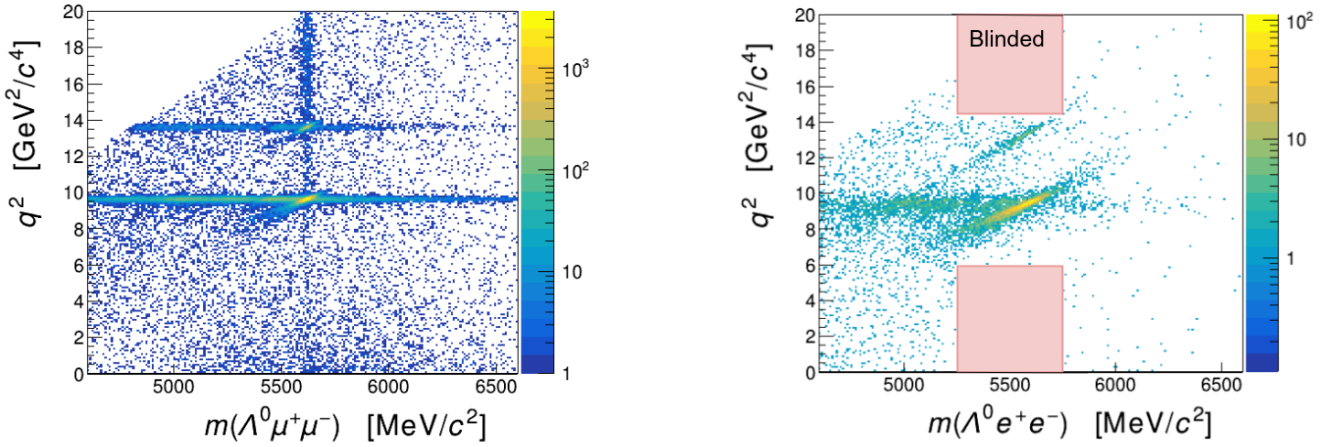

(a) (b)

Figure 10: q^2 vs $m(\Lambda^0 \ell^+ \ell^-)$ distributions for the muon mode (a) and electron mode (b) for the Run 2 dataset, after applying the combinatorial BDT (see Section 5.1).

Because of this overestimation, J/ψ and $\psi(2S)$ resonances are also reconstructed with a higher energy and can thus leak into the high-q^2 region. To prevent this, the definition of the high-q^2 region for the electron mode is based on the q^2_{track} variable, which is the reconstructed q^2 of the dilepton pair based only on their track information, without any bremsstrahlung added.

4.2 The single ratio and double ratio methods

Experimentally, the branching fraction of $\Lambda_b^0 \to \Lambda^0 \ell^+ \ell^-$ can be determined as follows:

$$\mathcal{B}(\Lambda_b^0 \to \Lambda^0 \ell^+ \ell^-) = \frac{N_{\Lambda_b^0 \to \Lambda^0 \ell^+ \ell^-}}{\epsilon_{\Lambda_b^0 \to \Lambda^0 \ell^+ \ell^-} \cdot \mathcal{L} \cdot \sigma_{\Lambda_b^0}}, \tag{4}$$

where N is the number of observed decays, ϵ is the total detection and reconstruction efficiency, $\mathcal{L}$ is the integrated luminosity of the data and $\sigma_{\Lambda_b^0}$ is the production cross-section of Λ_b^0. Using Equation 4, the single ratio method (denoted r) determines the ratio of branching fractions as:

$$r_\Lambda = \frac{\mathcal{B}(\Lambda_b^0 \to \Lambda^0 \mu^+ \mu^-)}{\mathcal{B}(\Lambda_b^0 \to \Lambda^0 e^+ e^-)} = \frac{N_{\Lambda_b^0 \to \Lambda^0 \mu^+ \mu^-}}{N_{\Lambda_b^0 \to \Lambda^0 e^+ e^-}} \cdot \frac{\epsilon_{\Lambda_b^0 \to \Lambda^0 e^+ e^-}}{\epsilon_{\Lambda_b^0 \to \Lambda^0 \mu^+ \mu^-}}, \tag{5}$$

where $\mathcal{L}$ and $\sigma_{\Lambda_b^0}$ are canceled out. However, there can still be systematic uncertainties that are not cancelled out effectively. These can be uncertainties related to the tracking and particle identification efficiencies, the trigger efficiencies or reconstruction efficiencies. In order to reduce these systematic uncertainties, a double ratio method (denoted R) is used:

$$\begin{aligned} R_\Lambda &= r_\Lambda \cdot r_{J/\psi}^{-1} \\ &= \frac{N_{\Lambda_b^0 \to \Lambda^0 \mu^+ \mu^-}}{N_{\Lambda_b^0 \to \Lambda^0 J/\psi(\to \mu^+ \mu^-)}} \cdot \frac{\epsilon_{\Lambda_b^0 \to \Lambda^0 J/\psi(\to \mu^+ \mu^-)}}{\epsilon_{\Lambda_b^0 \to \Lambda^0 \mu^+ \mu^-}} \cdot \frac{N_{\Lambda_b^0 \to \Lambda^0 e^+ e^-}}{N_{\Lambda_b^0 \to \Lambda^0 J/\psi(\to e^+ e^-)}} \cdot \frac{\epsilon_{\Lambda_b^0 \to \Lambda^0 J/\psi(\to e^+ e^-)}}{\epsilon_{\Lambda_b^0 \to \Lambda^0 e^+ e^-}}. \end{aligned} \tag{6}$$

Here, the single ratio r_Λ is taken and divided by the single ratio $r_{J/\psi}$. Using this method, systematic uncertainties in the ratio $\epsilon_{\Lambda_b^0 \to \Lambda^0 J/\psi(\to \ell^+ \ell^-)} / \epsilon_{\Lambda_b^0 \to \Lambda^0 \ell^+ \ell^-}$ can cancel out, as the $\Lambda_b^0 \to \Lambda^0 J/\psi(\to \ell^+ \ell^-)$ and $\Lambda_b^0 \to \Lambda^0 \ell^+ \ell^-$ decays (for each type of lepton) have similar kinematics and are reconstructed in similar fashion by the detector. This method reduces the systematic uncertainty on the total efficiency and hence reduces the uncertainty on R_Λ. The double ratio method does not introduce a deviation to R_Λ, as LFU for $r_{J/\psi}$ has already been established and is shown to be unity with sub-percent precision [28]:

$$r_{J/\psi}^{-1} = \frac{\mathcal{B}(J/\psi \to e^+ e^-)}{\mathcal{B}(J/\psi \to \mu^+ \mu^-)} = 0.9983 \pm 0.0078. \tag{7}$$

In the double ratio method, the J/ψ mode is referred to as the normalisation mode. Because the kinematics of these resonant modes are similar to the rare mode, and LFU has already been established for the resonant modes, the double ratio also allows us to perform cross-checks. These cross-checks can show us how certain cuts and other transformations on the data will affect the LFU ratio.

5 Backgrounds in $\Lambda_b^0 \to \Lambda^0 \ell^+ \ell^-$

After the selection of the $\Lambda_b^0 \to \Lambda^0 \ell^+ \ell^-$ candidates, the final signal-background separation is achieved by performing a fit to the reconstructed mass $m(\Lambda^0 \ell^+ \ell^-)$. The backgrounds that are still present in this fit are backgrounds arising from the mis-identification of particles, missing particle tracks in the reconstruction, combinatorial mismatch, leakage from other q^2 regions and combinations of all of the above. By studying the properties of these backgrounds, they can be modelled accordingly in the $m(\Lambda^0 \ell^+ \ell^-)$ fit.

5.1 The combinatorial background

The largest source of background is the combinatorial background. This background consists of events where particles are mistakenly combined to form a candidate $\Lambda_b^0 \to \Lambda^0 \ell^+ \ell^-$ decay, while not all its particles originally came from that decay. This type of background typically arises when random tracks or particles from unrelated decays are incorrectly assigned as potential decay products of the Λ_b^0 baryon. To model this background, a data sample is used consisting of $\Lambda_b^0 \to \Lambda^0 \ell^\pm \ell^\pm$ decays, where both leptons have the same sign. This decay is not allowed by the SM, as it violates lepton number conservation, hence any observations of this decay can only arise due to the mismatching of one (or both) same-sign lepton(s) to the rest of the decay. This same-sign data, together with MC $\Lambda_b^0 \to \Lambda^0 \ell^+ \ell^-$, is used to train a Boosted Decision Tree (BDT) to distinguish between the combinatorial data events and our signal events. The BDT is a form of a Multivariate Analysis which uses a set of input variables (like transverse momentum, PID scores, vertex quality etc.) to make a decision whether an event is likely to be signal or combinatorial background. It achieves this by recursively partitioning the dataset for each input variable and deciding if it overlaps more with the same-sign dataset or the MC signal dataset. The implementation and performance of this BDT on our data is still a work in progress by Chishuai Wang and is not part of this thesis. This combinatorial BDT is used to model the combinatorial background in the data analysed here.

5.2 Partially reconstructed backgrounds

Partially reconstructed backgrounds are backgrounds arising due to the exclusion of one or several particle tracks in the reconstruction. One such partially reconstructed background is $\Lambda_b^0 \to \Lambda_c^+ (\to \Lambda^0 \ell^+ \nu_\ell) \ell^- \overline{\nu}_\ell$, where the neutrinos and the intermediate Λ_c^+ state go undetected and hence are not included in the reconstruction of the decay. Because the final-state particles (that are detected) for partially reconstructed decays and our signal decay are the same, it is reconstructed as a $\Lambda_b^0 \to \Lambda^0 \ell^+ \ell^-$ decay. Since this specific partially reconstructed decay occurs at tree-level, its branching fraction is orders of magnitude larger than the $\Lambda_b^0 \to \Lambda^0 \ell^+ \ell^-$ branching fraction and depending on the q^2 region of interest the contribution of this background could be significant.

One way to look for this background in the data is by employing a Λ_c^+-veto. In the $\Lambda_b^0 \to \Lambda_c^+ (\to \Lambda^0 \ell^+ \nu_\ell) \ell^- \overline{\nu}_\ell$ decay, the invariant mass of the Λ^0 and ℓ^+ together will always be equal to or less than the mass of the Λ_c^+ baryon. This region ($m(\Lambda^0 \ell^+) \leq m(\Lambda_c^+)$) is therefore relatively rich in this background whereas the inverse region ($m(\Lambda^0 \ell^+) > m(\Lambda_c^+)$) should not contain any of these background events. Splitting the data this way and comparing these regions can give an insight in the contribution of this background in the total data sample.

Anther set of partially reconstructed backgrounds is $\Lambda_b^0 \to \Lambda^* (\to \Sigma^0 (\to \Lambda^0 \gamma) \pi^0) \ell^+ \ell^-$, where Λ^* is an excited Λ state. Due to the short lifetimes of Λ^* and Σ^0 and missing the photon and pion tracks in the reconstruction, this decay can be observed as a $\Lambda_b^0 \to \Lambda^0 \ell^+ \ell^-$ decay. This decay can occur for many Λ^* states, which are difficult to distinguish from one another in the data because the energies and momenta of neutral particles are challenging to reconstruct.

Another background, similar to these excited Λ states, are partially reconstructed decays that come from a Ξ_b baryon. These are $\Xi_b^0 \to \Xi^0 (\to \Lambda^0 \pi^0) \ell^+ \ell^-$ and $\Xi_b^- \to \Xi^- (\to \Lambda^0 \pi^-) \ell^+ \ell^-$. Similar to the Λ^* background, the tracks of the pions in these decays are not included in the reconstruction and hence the decay is reconstructed as $\Lambda_b^0 \to \Lambda^0 \ell^+ \ell^-$.

The Λ^* and Ξ_b decays are not as easily distinguishable from the rest of the data as the Λ_c^+ background. But there are still parameters in the data that could hint at an event corresponding to such a background decay. Examples of such parameters include momenta distributions, charge isolation variables (these quantify how isolated a particle is from other particles in its vicinity) and direction angle variables (the angle between the momentum vector of a

particle and the vector from the primary vertex to the secondary vertex). A combination of such variables could give a likelihood of an event being signal or a partially reconstructed background.

5.3 Backgrounds with misidentified particles

In the reconstruction process it can occur that a particle is identified as a different particle than it actually is. These misidentified particles can end up in the final selection. In the case of $\Lambda_b^0 \to \Lambda^0(\to p\pi^-)\ell^+\ell^-$ decays, it can occur that the identified proton was actually a pion that was misidentified as a proton. The final state then has a π^+ and a π^- instead of a p and a π^-. Because the mother particle of the decay is identified by its daughter particles, the decay is reconstructed as $\Lambda_b^0 \to \Lambda^0(\to p\pi^-)\ell^+\ell^-$, while the decay mode that actually took place is .

Although $\Lambda^0 \to p\pi^-$ and $K_S^0 \to \pi^+\pi^-$ are both two-body decays, they are fundamentally different when it comes to the momentum asymmetry between the two final state particles. This is because in the $\Lambda^0 \to p\pi^-$ case, the proton is significantly heavier than the pion, which affects the momentum distribution of the decay. This gives rise to a generally larger momentum asymmetry compared to the $K_S^0 \to \pi^+\pi^-$ case, where the average momentum asymmetry tends to be around zero, because of the equal mass of the pions (see Appendix A). On top of that, the $B^0 \to K_S^0(\to \pi^+\pi^-)\ell^+\ell^-$ decay can be identified by reconstructing $m(K_S^0\ell^+\ell^-)$, as this should yield a peak around the B^0 mass if the decay came from a B^0 meson. Using these methods, an estimate can be made of the background events that correspond to such a decay.

These misidentifications can also happen to the leptons in the $\Lambda_b^0 \to \Lambda^0\ell^+\ell^-$ decay, where the final state leptons are actually hadrons. This double misidentified background is of the form $\Lambda_b^0 \to \Lambda^0 h^+h'^-$, where h and h' can be different hadrons, which are both misidentified as leptons. This can occur in the RICH detectors due to overlapping Cherenkov angles for certain momentum ranges (Figure 7), but it can also occur in the ECAL. Electrons deposit most of their energy in the ECAL, while hadrons deposit energy in both the ECAL and HCAL. If a hadron deposits an unusually large fraction of its energy in the ECAL, it can mimic the energy deposition pattern of an electron. Other contributions to this background include track matching errors of hadron tracks to lepton tracks and decay in flight of pions and kaons. Pions and kaons can decay into muons and neutrinos before reaching the muon chambers. If the original hadron track is not well separated from the decay muon track, the muon might be wrongly associated with the hadron. These different contributions can lead to decays like $\Lambda_b^0 \to \Lambda^0 h^+h'^-$ being reconstructed as $\Lambda_b^0 \to \Lambda^0\ell^+\ell^-$.

5.4 Resonance leakage

As explained in Section 4, separating the analysis into different q^2 regions allows us to separate the resonant $\Lambda_b^0 \to \Lambda^0 J/\psi(\to \ell^+\ell^-)$ and $\Lambda_b^0 \to \Lambda^0\psi(2S)(\to \ell^+\ell^-)$ regions from the non-resonant $\Lambda_b^0 \to \Lambda^0\ell^+\ell^-$ mode. This separation however is not perfect. The q^2-cut can still allow the tails of the resonances to leak into the non-resonant regions. Because of the similarity between the resonant and non-resonant modes, there is no data-driven method to distinguish these (besides the already applied q^2 cuts). It is however still possible to estimate how many of these resonant events leak into the non-resonant mode by using MC data. MC data can tell us the fraction of J/ψ and $\psi(2S)$ decays that leak into the rare mode. Scaling this fraction by the number of observed $\Lambda_b^0 \to \Lambda^0\psi(2S)$ (or $\Lambda_b^0 \to \Lambda^0 J/\psi$) decays can therefore give us an absolute estimate of the amount of background that leaks into the rare mode.

6 Results & Discussion

Firstly, an estimation is made using branching fractions and efficiencies to calculate how much background we expect to see in the data. These are referred to as expected yields, and their values are analysed and discussed. Secondly, using MC samples and the same-sign data set, the different background components are modelled and fitted to the data. Finally, two data-driven methods are employed. One method serves to find the amount of $B^0 \to K^0_S(\to \pi^+\pi^-)\mu^+\mu^-$ background in the data. The other method serves to find the amount of $\Lambda^0_b \to \Lambda^+_c(\to \Lambda^0\mu^+\nu_\mu)\mu^-\overline{\nu}_\mu$ background present in the data.

6.1 Expected background yields

Taking a ratio of Equation 4, the expected yield of a background with respect to signal can be calculated as:

$$\frac{N_{\text{bkg}}}{N_{\text{sig}}} = \frac{\sigma_{\text{bkg}}}{\sigma_{\text{sig}}} \cdot \frac{\mathcal{B}(\text{bkg})}{\mathcal{B}(\text{sig})} \cdot \frac{\epsilon_{\text{bkg}}}{\epsilon_{\text{sig}}}, \tag{8}$$

where the ratio $N_{\text{bkg}}/N_{\text{sig}}$ is a measure of the number of reconstructed background events over the number of reconstructed signal events. This expected yield is calculated by using known branching fractions ($\mathcal{B}$) and production cross-sections (σ), together with efficiencies (ϵ). The branching fractions and production cross-sections of the various background decays and the signal decay are taken from PDG [28]. The efficiencies are a measure of the fraction of events that made it through the entire detection and reconstruction process (as described in Figure 8).

The efficiencies are calculated using MC samples for each type of background (and signal) decay. The total efficiency of a decay is the product of the generator level efficiency and the reconstruction and selection efficiency. The generator level efficiency refers to the efficiency of generating events that fall within the LHCb detector acceptance, before any detector effects or reconstruction algorithms are applied. The reconstruction and selection efficiency refers to the fraction of events that are successfully reconstructed by the detector and pass the reconstruction and selection algorithms. The code used to calculate these efficiencies is further explained in Appendix B.2. The reconstruction and selection efficiencies also include the effects of LL and DD cuts, q^2 cuts, the combinatorial BDT and other transformations that we apply to the data in the analysis stage.

Using Equation 8, the following background yields are obtained in the high-q^2 region (after applying the combinatorial BDT):

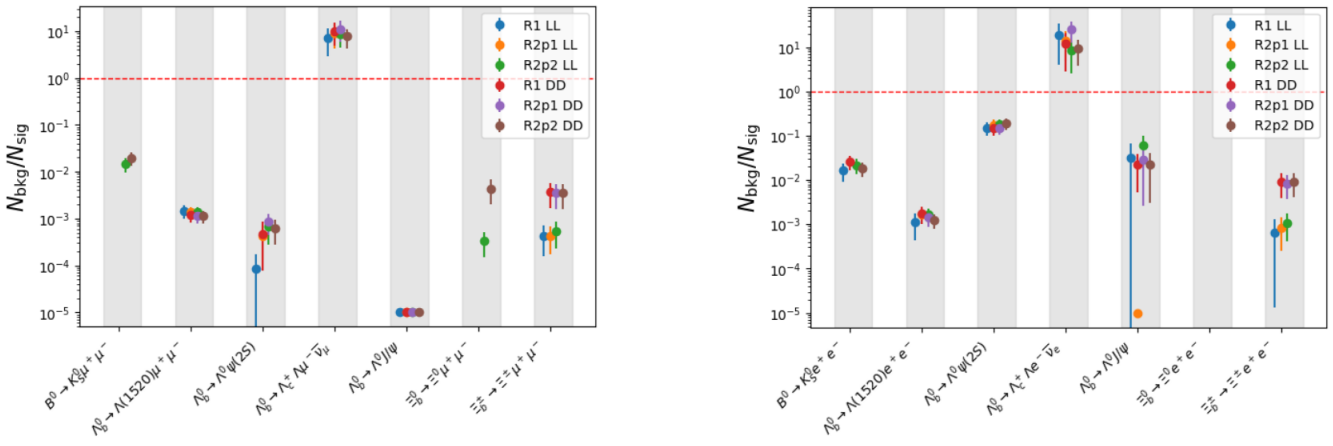

(a) Muon mode

(b) Electron mode

Figure 11: Contributions of different backgrounds with respect to signal for each run and track type, calculated using Equation 8.

Tables with more specific values of these background contributions and the values of the branching fractions and efficiencies used are included in Appendix C. Details on the code used to calculate these yields are found in Appendix B.1. Some MC samples were not available for these runs at the moment and hence the efficiencies and yields could not be calculated, these entries are not included in Figure 11. Some efficiencies were found to be zero, due to the limited statistics of the MC samples. In Figure 11, these are set to a value of 10^{-5}.

Since not all branching fractions for the electron mode are known, the same branching fractions (and uncertainties) are assumed for the electron mode. The efficiencies however are different and hence this leads to different expected background yields. The estimates for the electron mode do not yet use the q^2_{track} cut, and the efficiencies are calculated using the full (including bremsstrahlung) q^2 cut instead. Using this cut makes the resonant modes far more abundant in the high-q^2 region.

Most backgrounds seem to be contributing the same amount in both the LL and DD cases, except for the $\Xi_b^- \to \Xi^-(\to \Lambda^0\pi^-)\ell^+\ell^-$ and $\Xi_b^0 \to \Xi^0(\to \Lambda^0\pi^0)\ell^+\ell^-$ backgrounds. Although not all MC samples were available for the $\Xi_b^- \to \Xi^-(\to \Lambda^0\pi^-)\ell^+\ell^-$ sample, the two data points in the muon mode imply that this charged background follows the same trend as the neutral $\Xi_b^0 \to \Xi^0(\to \Lambda^0\pi^0)\ell^+\ell^-$ background, where it is almost an order of magnitude more abundant in the DD case as opposed to the LL case. The $\Xi^\pm$ (or Ξ^0) and Λ^0 both have mean lifetimes in the order of 10^{-10} s [28], hence the time it takes for a $\Xi_b^- \to \Xi^-(\to \Lambda^0\pi^-)\ell^+\ell^-$ decay (or $\Xi_b^0 \to \Xi^0(\to \Lambda^0\pi^0)\ell^+\ell^-$ decay) to produce a proton-pion pair is significantly longer than the time it takes for a $\Lambda_b^0 \to \Lambda^0(\to p\pi^-)\ell^+\ell^-$ decay to produce a proton-pion pair, making it more likely for this background to only leave hits in the TT and T-stations, resulting in more DD tracks as opposed to LL tracks. This effect is not seen in the other partially reconstructed backgrounds, as the mean lifetimes of Λ^*, Λ_c^+ and Σ^0 are orders of magnitude lower than the mean life of Λ^0.

The yields for the Λ_c^+ background show an estimation for the $\Lambda_b^0 \to \Lambda_c^+(\to \Lambda^0\ell^+\nu_\ell)\ell^-\overline{\nu}_\ell$ background that is orders of magnitude higher than the other backgrounds. This is likely an overestimation. It was found that the $m(\mu^-\overline{\nu}_\mu)$ distribution from the MC sample (Appendix E) does not align with the $m(\mu^-\overline{\nu}_\mu)$ distribution found in data [29]. This, and perhaps other biases in the MC could result in a higher efficiency than we actually observe. The branching fraction ratio of this decay is orders of magnitude larger than the other backgrounds (Appendix A). Although it stands out, it is in line with the SM. The branching fractions taken for this decay are all full branching fractions, well known and taken from PDG.
Some other branching fraction estimations for partially reconstructed backgrounds could be estimated lower than they actually are, as some of their branching fractions are only known partially or with respect to other decay modes, which is not fully accounted for. The partially reconstructed backgrounds all seem to have a low contribution, but their accumulative effect might be significant. This is also considering the fact that not all Λ^* states are represented here (only the $\Lambda(1520)$ decay). A method to model such partially reconstructed backgrounds is by employing a BDT for this category, as all these backgrounds have similar properties:

- Particles are not reconstructed, so energy and momentum are missing.
- Other particles that were part of the decay could be present in the vicinity of the decay products, this can be checked using charge isolation variables.
- Direction angles (the angle between the momentum vector of a particle and the vector from the primary vertex to the secondary vertex) could be larger for partially reconstructed decays.

These properties can be studied and a BDT can be trained to model this type of background. This method is also employed in the currently ongoing $R(K)$ high-q^2 analysis.

Another background that stands out is $\Lambda_b^0 \to \Lambda^0\psi(2S)(\to \ell^+\ell^-)$, as it is much more present in the electron mode than the muon mode. This decay has a branching fraction relative to signal around 1, implying that the branching fractions are about equal. The reason for this is that although the branching fraction of the resonant mode is orders of magnitudes higher than the rare mode, the branching fraction of $\psi(2S) \to \ell^+\ell^-$ is only of order 10^{-3} [28], which brings down the total branching fraction to be of the same order as the rare mode.

The result of the high resonance leakage in the electron mode originates from the lower momentum resolution. This is mostly due to bremsstrahlung losses and recovery, due to which the resonant mass is often under- or overestimated. In order to reduce the resonant leakage into the electron mode, a 14.3 $\text{GeV}^2/c^4 < q^2_{\text{track}} < 20.0$ GeV^2/c^4 cut should be introduced instead of the normal q^2 cut. A study should be performed on the effectiveness of such a cut, while keeping enough statistics to perform the analysis.

Lastly, no estimation for the double misidentified background $\Lambda_b^0 \to \Lambda^0 h^+ h'^-$ was given. An estimate could be made using MC samples of $\Lambda_b^0 \to \Lambda^0 K\pi$, $\Lambda_b^0 \to \Lambda^0 \pi\pi$ or $\Lambda_b^0 \to \Lambda^0 KK$ decays, as pions and kaons are most abundantly produced in the LHCb detector. A similar estimate could be made using branching fractions and efficiencies when the MC samples and generator level efficiencies are available. The number of events of this background in the data will likely be higher than this estimate would give, as there are also many other hadrons produced in the LHCb detector that could also be misidentified as leptons. Therefore data-driven method needs to be found to quantify and model (and/or filter for) this background.

6.2 $m(\Lambda^0\ell^+\ell^-)$ distributions

Because the data is a cumulative effect of all the background and signal decays, MC samples consisting of these individual decays can be used to model the data. The events of each MC sample that make it through the entire selection and reconstruction process are used to determine $m(\Lambda^0\ell^+\ell^-)$. The same-sign data set is used to model the combinatorial background component. A fit is performed through the $m(\Lambda^0\ell^+\ell^-)$ distribution of each MC sample (and the same-sign data set), representing the contribution of each background. The resulting curve and its fit parameters are saved and used in a combined fit to the data. In this combined fit, the shape of each background contribution is maintained, while its amplitude is allowed to vary. The results of such a fit are shown in Figure 12 and the resulting background yields obtained from this method are summarized in Table 3. The electron mode is not shown, as it has to remain blinded.

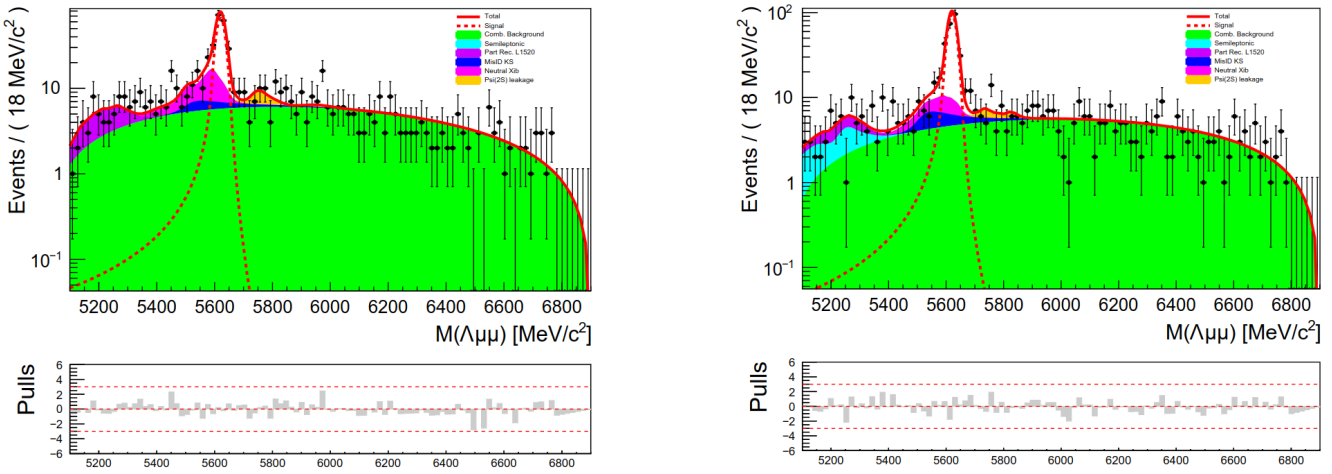

(a) LL

(b) DD

Figure 12: $m(\Lambda^0\mu^+\mu^-)$ distribution of R2p2 data, fitted using MC samples of the different background components. The combinatorial background is modelled using the same-sign data set. These are the results after the combinatorial BDT has been applied. The different background yields are left floating, meaning they can take any value to find the best fit.

Floating yields muon mode			
Decay mode	Colour in plot	Yield (# events)	
		LL	DD
$\Lambda_b^0 \to \Lambda^0\mu^+\mu^-$	red (dotted)	159.2	225.6
Combinatorial background	green	407.8	378.3
$\Lambda_b^0 \to \Lambda_c^+(\to \Lambda^0\mu^+\nu_\mu)\mu^-\overline{\nu}_\mu$	mint blue	0.0	23.2
$\Lambda_b^0 \to \Lambda^*(\to \Sigma^0(\to \Lambda^0\gamma)\pi^0)\mu^+\mu^-$	purple	28.0	14.6
$B^0 \to K_S^0(\to \pi^+\pi^-)\mu^+\mu^-$	dark blue	21.6	28.9
$\Xi_b^- \to \Xi^-(\to \Lambda^0\pi^-)\mu^+\mu^-$	pink	63.5	30.3
$\Lambda_b^0 \to \Lambda^0\psi(2S)(\to \mu^+\mu^-)$	yellow	15.1	9.1

Table 3: Number of events of each background in the R2p2 data, found by applying a fit to the $m(\Lambda^0\mu^+\mu^-)$ distribution. The yields of each background component are left floating. This means they are allowed to take any value in order to find the best fit to the data.

In the above fit, the yields of each background component are allowed to take any value in order to find the best fit. It can be seen that this does not give consistent results for the LL and DD modes, as some backgrounds (for example $\Lambda_b^0 \to \Lambda_c^+(\to \Lambda^0\mu^+\nu_\mu)\mu^-\overline{\nu}_\mu$) have a higher contribution in one of these modes over the other. These results are also not consistent with the yields from Figure 11. Using many background contributions as shown in Figure 12 gives the fit too many free parameters. This results in an overfit, which is not a realistic representation of the actual backgrounds present in the data.

In order to force the yields to be consistent with the yields obtained in Figure 11, the same fitting method is used but the yields are only allowed to take values that are consistent with the yields from Figure 11 within 3 standard deviations. These results are shown in Figure 13 and Table 4.

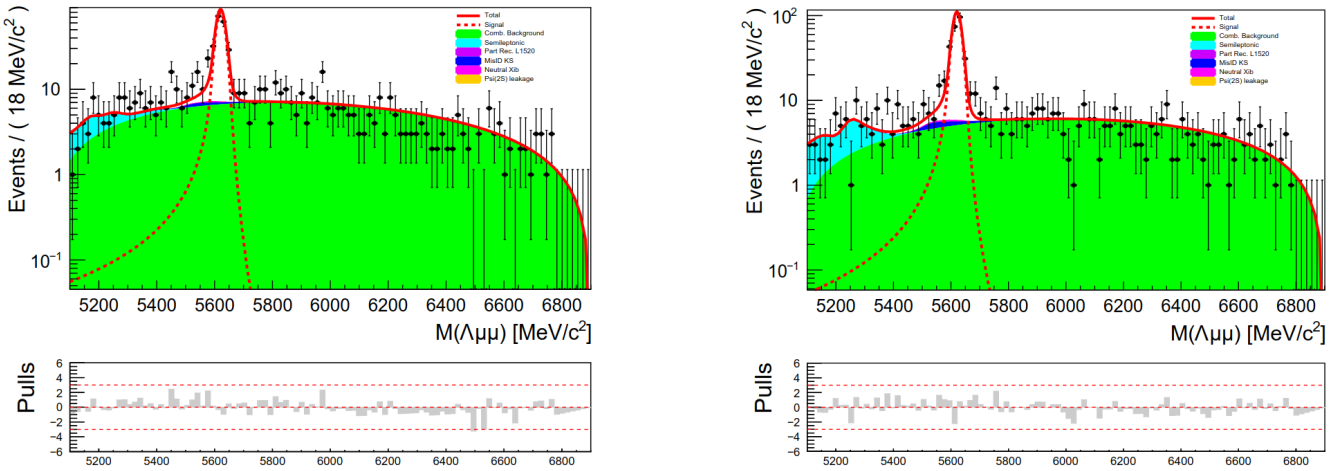

(a) LL

(b) DD

Figure 13: $m(\Lambda^0\mu^+\mu^-)$ distribution of R2p2 data, fitted using MC samples of the different background components. The combinatorial background is modelled using the same-sign data set. These are the results after the combinatorial BDT has been applied. The yields of each background component can only vary within 3 standard deviations of the result in Figure 11.

Limited yields muon mode			
Decay mode	Colour in plot	Yield (# events)	
		LL	DD
$\Lambda_b^0 \to \Lambda^0\mu^+\mu^-$	red (dotted)	192.2	249.4
Combinatorial background	green	471.6	413.0
$\Lambda_b^0 \to \Lambda_c^+(\to \Lambda^0\mu^+\nu_\mu)\mu^-\overline{\nu}_\mu$	mint blue	21.2	35.0
$\Lambda_b^0 \to \Lambda^*(\to \Sigma^0(\to \Lambda^0\gamma)\pi^0)\mu^+\mu^-$	purple	0.4	0.5
$B^0 \to K_S^0(\to \pi^+\pi^-)\mu^+\mu^-$	dark blue	7.2	9.4
$\Xi_b^- \to \Xi^-(\to \Lambda^0\pi^-)\mu^+\mu^-$	pink	1.8	2.3
$\Lambda_b^0 \to \Lambda^0\psi(2S)(\to \mu^+\mu^-)$	yellow	0.3	0.4

Table 4: Number of events of each background in the R2p2 data, found by applying a fit to the $m(\Lambda^0\mu^+\mu^-)$ distribution. The yields of each background component can only vary within 3 standard deviations of the result in Figure 11.

The pulls below the plots show the difference between the unbinned fit and the number of events in the bin centered around that point in the fit, measured in standard deviations. The standard deviation of each bin (the error bars) are determined using Poisson statistics. Using these pulls, it can be seen that for the limited yields case, the fit deviates more around the signal region. It is possible that in this region, there is an additional background present that is not taken into account, or that one of the backgrounds modelled should have a larger contribution in this region that we have allowed it to. This is likely a partially reconstructed decay, as not all Λ^* states are modelled and neither is the $\Xi_b^0 \to \Xi^0(\to \Lambda^0\pi^0)\mu^+\mu^-$ decay, which are also likely in this region due to their similarities to the $\Lambda(1520)$ and $\Xi_b^\pm$ backgrounds.

6.3 K^0_S misID contribution in data

To separate the $B^0 \to K^0_S(\to \pi^+\pi^-)\ell^+\ell^-$ background (and other $K^0_S \to \pi^+\pi^-$ contributions) from our data, a K^0_S-veto has been developed. This veto uses the difference in momentum asymmetry between the proton-pion pair that come from the Λ^0 decay and the momentum asymmetry between the pion-pion pair that come from the K^0_S decay. This veto is shown in Figure 14. The variable that is cut by this veto is plotted on the x-axis, and is given by:

$$x_{\text{ksveto}} = -\frac{m(\Lambda^0)}{400} + 1 + \frac{|p_\pi|}{|p_p|}, \tag{9}$$

where p_π and p_p are the pion and proton momenta respectively. A more detailed explanation of the origin of this variable is given in Appendix A.

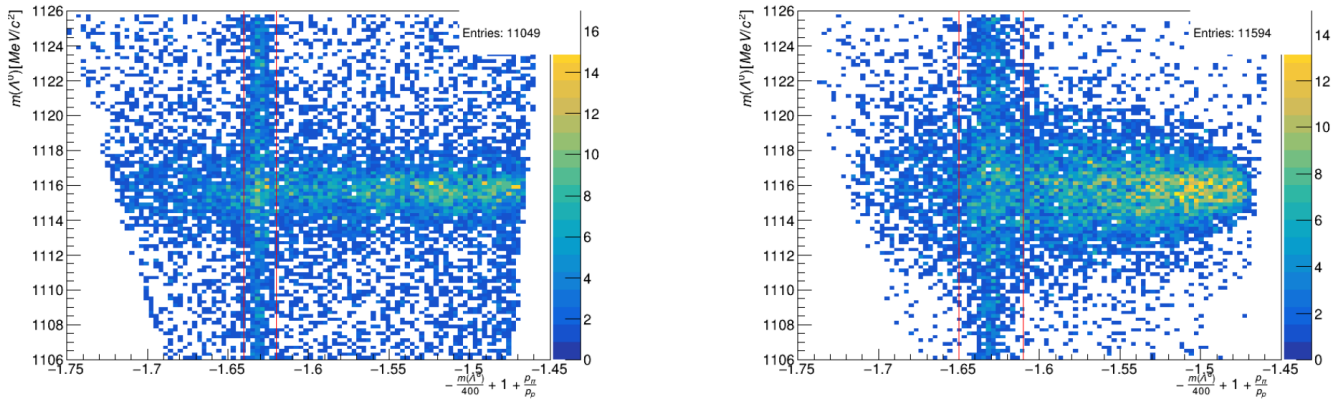

(a) LL (b) DD

Figure 14: Plots of x_{ksveto} versus $m(\Lambda^0)$, outlining the momentum asymmetry differences between the $\Lambda^0_b \to \Lambda^0(\to p\pi^-)\mu^+\mu^-$ and $B^0 \to K^0_S(\to \pi^+\pi^-)\mu^+\mu^-$ decay modes in the R2p2 data set.

The K^0_S-veto is then defined as $-1.64 < x_{\text{ksveto}} < -1.62$ for LL candidates and $-1.65 < x_{\text{ksveto}} < -1.61$ for DD candidates. The distribution for the LL candidates is narrower due to better estimation of the pion and proton momenta. The data shown here however, also contains a significant portion of combinatorial data. This is not just combinatorial background from the mismatch of hadrons or leptons in the $\Lambda^0_b \to \Lambda^0(\to p\pi^-)\mu^+\mu^-$ decay, but also from the mismatch of hadrons or leptons in the $B^0 \to K^0_S(\to \pi^+\pi^-)\mu^+\mu^-$ decay. Using the combinatorial BDT, both these backgrounds can largely be filtered out. Of the remaining data, the $m(K^0_S\mu^+\mu^-)$ mass is reconstructed. The amount of $B^0 \to K^0_S(\to \pi^+\pi^-)\mu^+\mu^-$ background is then given by the number of events around the B^0 mass. This is still a conservative estimate, as it also contains some combinatorial and $\Lambda^0_b \to \Lambda^0\mu^+\mu^-$ events.

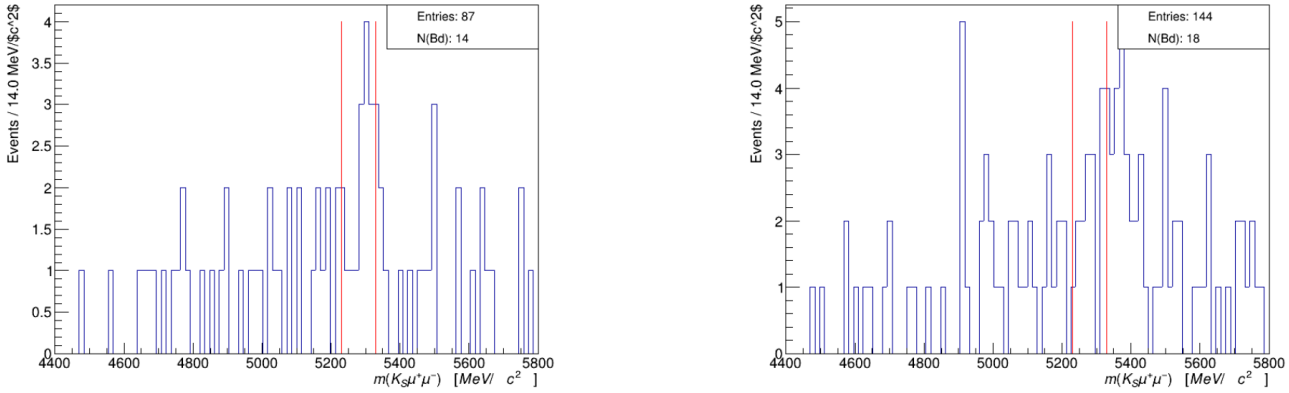

(a) LL (b) DD

Figure 15: Plots of $m(K^0_S\mu^+\mu^-)$ of the R2p2 dataset, where the red bars are placed at $m(B^0) \pm 50$ MeV/c^2.

The peak slightly to the right of the B^0 mass is actually a shifted peak of the Λ_b^0 mass. Because of this overlap, many events within the chosen region could even come from our signal, and taking the number of events within the B^0 mass window is already an overestimation of the $B^0 \to K_S^0(\to \pi^+\pi^-)\mu^+\mu^-$ background. This background comes out as 14 out of 710 total events for the LL sample and 18 out of 724 events for the DD sample.

The $B^0 \to K_S^0(\to \pi^+\pi^-)\ell^+\ell^-$ background contribution as observed in the data is in agreement with its expected yield (around 2%). Figure 14 might suggest there is significantly more of this background present, but the majority of the data that lie within the K_S^0-veto is actually combinatorial. This background is non-peaking at $m(B^0)$ and is also present in the same-sign ($\Lambda_b^0 \to \Lambda^0\ell^\pm\ell^\pm$) data set. Because the main contribution is of a combinatorial nature and the same-sign data is used to model this combinatorial background, it is already accounted for. This background (and its combinatorial variety) can also be filtered out entirely, but the disadvantage is that this also cuts signal events. A study should be performed on whether this veto is advantageous or not.

6.4 Semileptonic Λ_c^+ decay contribution in data

The R2p2 dataset is taken and the combinatorial BDT is applied to the data. The $\Lambda_b^0 \to \Lambda_c^+(\to \Lambda^0\mu^+\nu_\mu)\mu^-\overline{\nu}_\mu$background is separated from the rest of the data by employing a Λ_c^+-veto, as all contributions from this background should have $m(\Lambda^0\mu) < m(\Lambda_c^+)$, where the charge of the muon has the same charge as the charge of the proton from the Λ^0. This veto is shown in Figure 16.

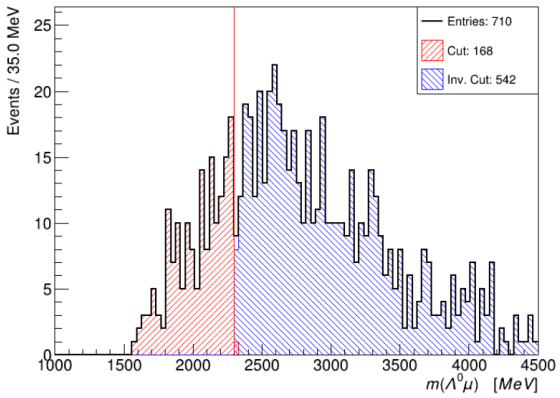

(a) R2p2, track LL

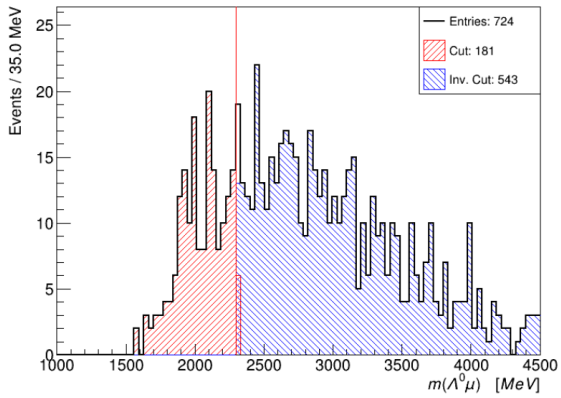

(b) R2p2, track DD

Figure 16: Plots showing the reconstructed $\Lambda^0\mu$ mass, with the data separated by the Λ_c^+ mass. The Λ_c^+-veto is applied on the LL and DD data of R2p2, after the combinatorial BDT is applied.

Comparing the data to MC samples of $\Lambda_b^0 \to \Lambda_c^+(\to \Lambda^0\mu^+\nu_\mu)\mu^-\overline{\nu}_\mu$ and $\Lambda_b^0 \to \Lambda^0\mu^+\mu^-$ shows that the data follows a similar distribution to the signal MC (shown in Appendix D.1). The DD sample is however more peaking than the LL sample, which could indicate that more of this background is present in the DD sample. Figure 16 does show a slight peaking region around 2000 MeV. These events could correspond to the Λ_c^+ background, however due to the low statistics and fluctuations in this area it is difficult to estimate how many events there are. The peaking behaviour is not consistent with being orders of magnitude larger than the signal component, as estimated in Figure 11, as such a contribution would be much more prominent.

For both data samples, the Λ_b^0 mass is also reconstructed and shown in Figure 17.

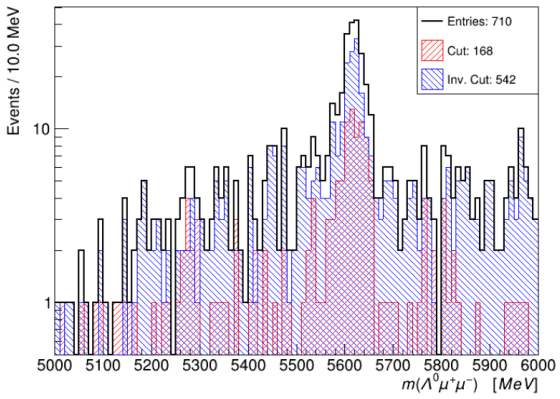

(a) R2p2, track LL

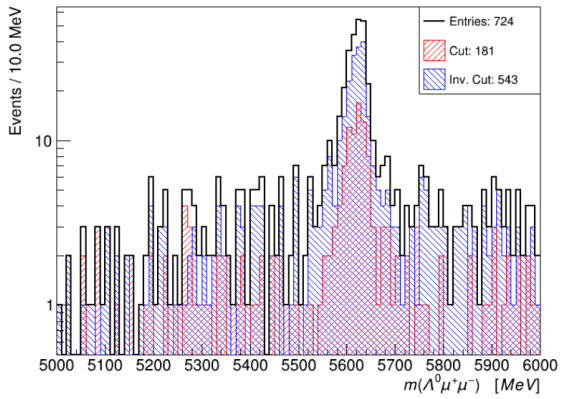

(b) R2p2, track DD

Figure 17: Reconstruction of $m(\Lambda^0\mu^+\mu^-)$ of R2p2 data. The data in red corresponds to the events that have a reconstructed $\Lambda^0\mu$ mass lower than the Λ_c^+ mass and the data in blue have a reconstructed $\Lambda^0\mu$ mass above the Λ_c^+ mass.

The shapes however of both distributions in Figure 17 are fairly similar. A Λ_c^+ background would have a contribution to the lower end of the $m(\Lambda^0\mu^+\mu^-)$ spectrum, which is not significantly more prominent in the data in red compared to the data in blue.

The Λ_c^+-veto could be used to filter out the Λ_c^+ background entirely, however such a veto is likely not necessary in the high q^2 region, as there is no significant contribution of this background here. Both sides of the Λ_c^+-veto show a similar shape in the $m(\Lambda^0\mu^+\mu^-)$ distribution. This background can be further quantified by performing a fit of the combinatorial background and signal components on the inverse cut (blue side) data in Figure 17. The resulting fit parameters can be used to perform a fit on the cut (red side) data, with an additional component to model the Λ_c^+ background. Because these two sides should be similar apart from this background, the yield of the Λ_c^+ component can therefore be an accurate representation of the amount of this background present in the data. This amount will likely be of the order of a couple percent to 10 percent with respect to signal, as this component is not clearly visible by eye in Figure 16.

7 Conclusion & Outlook

The measurement of $R(\Lambda)$is faced with challenges due to its low statistics, and hence it is vital to understand its backgrounds. These backgrounds consists of different types, namely the combinatorial background, partially reconstructed backgrounds, backgrounds due to mis-identified particles and resonance leakage. Using branching fractions from PDG and efficiency calculations using MC samples, expected yields for these backgrounds are determined (aside from the combinatorial background, which is another project in itself). These show that most backgrounds should be equally present in the LL sample as the DD sample, aside for the $\Xi_b^- \to \Xi^-(\to \Lambda^0\pi^-)\ell^+\ell^-$ and $\Xi_b^0 \to \Xi^0(\to \Lambda^0\pi^0)\ell^+\ell^-$ backgrounds.
$\Xi_b^- \to \Xi^-(\to \Lambda^0\pi^-)\ell^+\ell^-$ and $\Xi_b^0 \to \Xi^0(\to \Lambda^0\pi^0)\ell^+\ell^-$ backgrounds are much more present in the DD sample as opposed to the LL sample due to the mean lifetime of the Ξ baryon being the same order of magnitude as the mean lifetime of the Λ^0 baryon. This effect can be further investigated once more MC samples are available.
This type of background, as well as the other partially reconstructed backgrounds, is best studied using a BDT, trained using momentum and energy distributions, charge isolation variables and direction angle variables. It is estimated that these backgrounds individually might not have a significant contribution, but with this method they can be described cumulatively, which might be a non-negligible contribution.

The estimates show that the semileptonic $\Lambda_b^0 \to \Lambda_c^+(\to \Lambda^0\ell^+\nu_\ell)\ell^-\overline{\nu}_\ell$ background should be most abundant. However, inspecting the data reveals that this background is not as significant in the high-q^2 region as estimated. However, this background can still be present and Figures 16 show slight peaking behaviour. This background can be further quantified by fitting a combinatorial background and signal shape for the Λ_c^+-vetoed region (without Λ_c^+ background present), and using these fit parameters to perform a fit plus a Λ_c^+ background component in the inverse vetoed region (the region with all the Λ_c^+ background present).

The $B^0 \to K_S^0(\to \pi^+\pi^-)\ell^+\ell^-$ background is shown to be in agreement with expectations, about 2.0% w.r.t. signal. There is however a large combinatorial contribution of this background, which is already modelled accordingly. This background, together with its combinatorial component, can be cut out by using a K_S^0-veto. A future study should show whether this is desirable, as it negatively impacts the statistics of the signal, but could potentially help in reducing this background and its combinatorial counterpart.

For the electron mode, resonance leakage is a significant effect. The analysis presented does not cut the high-q^2 region on the q^2_{track} variable. This could cut out this background contribution entirely, but will likely also negatively impact the already low statistics. Studies should be performed on the effects of such a cut.

One other type of background is yet to be investigated, which consists of hadrons, being misidentified as leptonsin a $\Lambda_b^0 \to \Lambda^0 h^+ h'^-$ decay, where h and h' can be different hadrons.

8 Acknowledgements

I would like to express my gratitude to a number of people, not only to those who helped me directly in my work but also to those making the research environment at KVI enjoyable and supported me personally during my MSc research project.

First and foremost I would like to express my deepest gratitude to my supervisor Mick Mulder. Thanks for always being available for all my questions, even in absurd hours of the day. Thanks for your commitment and enthusiasm in explaining all kinds of physics concepts to me (and Max). I see that he already mentioned it in his acknowledgements but he is completely right in stating that you might be the best supervisor a student could wish for. I don't think many supervisors are as committed to their students as you are, and we deeply appreciate it.

I would like to extend my gratitude to Niladri Sahoo and Chishuai Wang. I could not always follow your discussions, especially when I first started out. I appreciate you for trying to make them understandable to me and for helping me in my project. Thanks for answering all the (sometimes dumb) questions I had. I learned a lot from you guys, thank you for that.

My other thanks go out to all my LHCb Groningen colleagues, but I want to thank Max Wiegertjes, Jan de Boer and Andrej Sarnatskiy specifically. Thank you Max and Jan for the mostly insightful and sometimes not so insightful (but still fun) discussions. It was very enjoyable sharing an office/canteen with you Jan and Max and if it wasn't for you I probably would not show up at 9:00h most of the time.

Thank you Andrej for the enjoyable time at CERN and the enjoyable time in Groningen. Thanks for taking the initiative to organise fun events like dinner, pool/biljards and bouldering. Good luck with your PhD!

A Armenteros-Podolanski plots

The Armenteros-Podolanski plot is a widely used method to separate $K^0_S \to \pi^+\pi^-$ from $\Lambda^0 \to p\pi^-$. The Armenteros-Podolanski plot is constructed by plotting the transverse momentum of a daughter particle versus the longitudinal momentum asymmetry of the daughter particles, defined as

$$\alpha = \frac{p^+_{\text{ortho}} - p^-_{\text{ortho}}}{p^+_{\text{ortho}} + p^-_{\text{ortho}}}, \tag{10}$$

where $p^\pm_{\text{ortho}}$ denotes the momentum component of the daughter particle of charge $\pm$ in the longitudinal direction of the direction of flight of the mother particle.

K^0_S mesons, decaying into two pions, generally populate a region where the transverse momentum p_T is higher because the mass difference between the 2 pions and the K^0_S is larger than the mass difference between the proton-pion pair coming from a Λ^0 baryons. The distribution of α is symmetric around zero for a kaon decaying into two pions because the pions are equal in mass. For Λ^0 baryons decaying into a proton and a pion on the other hand, the α distribution tends to be nonzero due to the higher proton mass. Because α is defined by the charges of the particles and not their identities, the plot splits the $\Lambda^0 \to p\pi^-$ and $\overline{\Lambda^0} \to p^-\pi^+$ decays.

Figure 18 shows the Armenteros-Podolanski plots of the signal and background using MC samples for $\Lambda^0_b \to \Lambda^0(\to p\pi^-)\mu^+\mu^-$ and $B^0 \to K^0_S(\to \pi^+\pi^-)\mu^+\mu^-$.

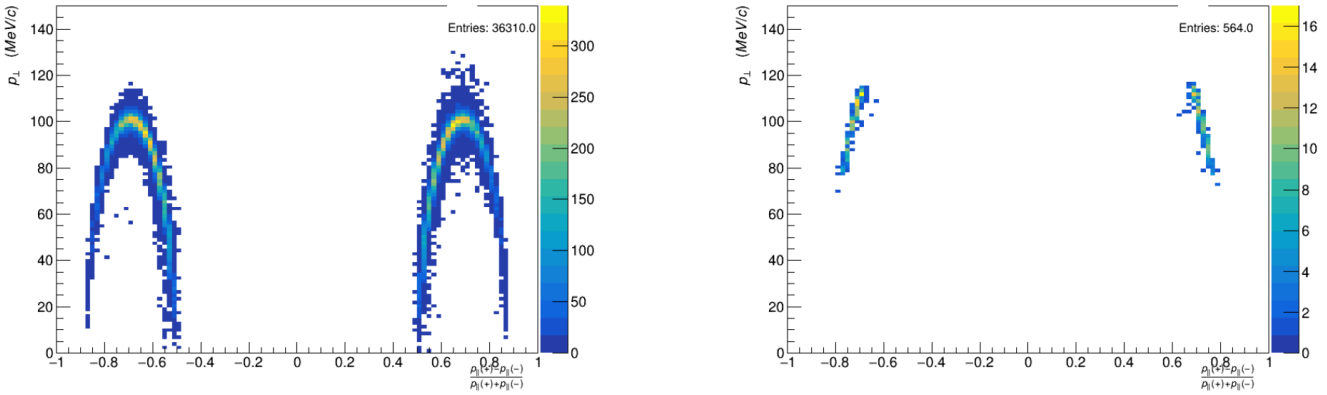

(a) $\Lambda^0_b \to \Lambda^0(\to p\pi^-)\mu^+\mu^-$

(b) $B^0 \to K^0_S(\to \pi^+\pi^-)\mu^+\mu^-$

Figure 18: Armenteros-Podolanski plots of MC data of R2p2, LL tracks. The momentum asymmetry α is plotted versus the transverse momentum of the daughter particles.

In the $R(\Lambda)$ analysis, the reconstructed mass of the daughter particles is required to be within range of the Λ^0 mass. This indirectly puts a constraint on the transverse momentum of its daughter particles, hence the $B^0 \to K^0_S(\to \pi^+\pi^-)\mu^+\mu^-$ sample is cut off for higher transverse momentum. Without this cutoff, the shape in (b) would form a semi-elliptical shape, distinctive of K^0_S mesons. In the data, the shapes of these contributions overlap, as shown in Figure 19.

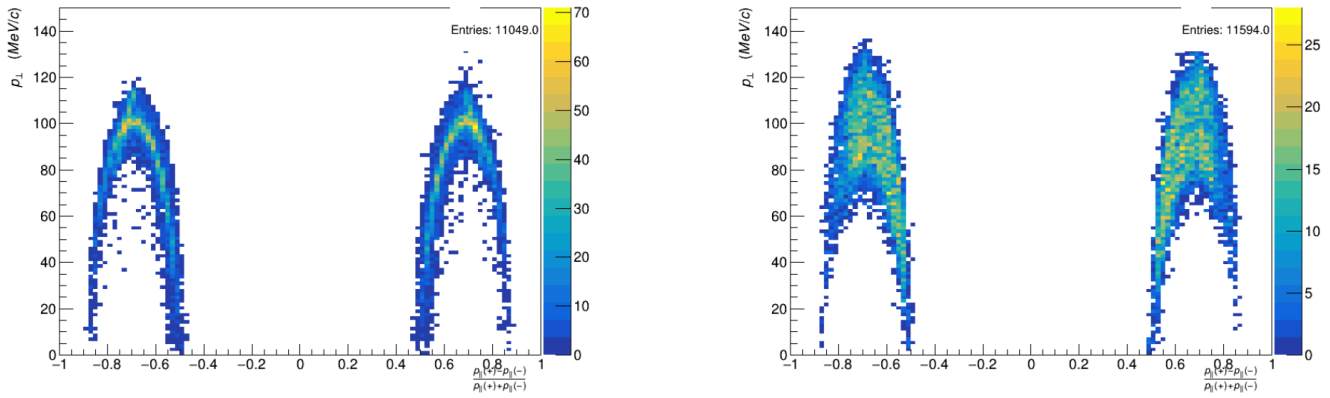

(a) Data (LL)

(b) Data (DD)

Figure 19: Armenteros-Podolanski plots of R2p2 data. The momentum asymmetry α is plotted versus the transverse momentum of the daughter particles.

In the $R(\Lambda)$ analysis, the Armenteros-Podolanski method is slightly altered to construct a plot that we can perform a cut on to separate the K^0_S contributions from the rest of the data. Firstly, the data is not plotted with respect to the direction of flight of the mother particle, but it is transformed to use the ratio of total momentum of the pion and proton on the x-axis, and $m(\Lambda^0)$ on the y-axis. The resulting plot would still give shape where the K^0_S and Λ^0 contributions diagonally overlap, so in order to make these contributions perpendicular, a factor proportional to the y-axis is added. In the end the resulting plot is a $m(\Lambda)$ versus $m(\Lambda)/400 + 1 - p_\pi/p_p$ plot.

B Python scripts used

All scripts and functions used are stored in the RLambda Gitlab:

`https://gitlab.cern.ch/LHCb-RD/ewprlambda`

B.1 Expected yields

The expected yields are calculated using Equation 8, for which the branching fractions and efficiencies of the different background and signal modes are needed. The code used to calculate this is stored in the folder:

`/ewprlambda/Studies/QsqHigh_backgrounds/ExpectedYields/`

This folder contains a couple files:

- `YieldEstimationsEE.yaml`
  A yaml file containing all the values of relative branching fractions and efficiencies for the electron mode.
- `YieldEstimationsEE.yaml`
  A yaml file containing all the values of relative branching fractions and efficiencies for the electron mode.
- `BranchingFractions.json`
  This file stores the branching fractions and uncertainties that are used to calculate the branching fraction ratios with respect to signal. For each entry, it contains a weblink to the reference it is taken from and sometimes I left a comment describing what value is taken or how it is derived.

- `YieldEstimations.py`
  This file can be run in the terminal by specifying which analysis mode to use (MM or EE for muon or electron mode respectively). It contains a list of tuples for these analysis modes. These are the backgrounds it will iterate over. The script reads out the branching fractions it needs from `BranchingFractions.json` to calculate the relative branching fractions of each background with respect to signal. These relative branching fractions are defined inside this python script and can easily be checked /altered if needed. The efficiencies used in the yield estimation are not determined by this script, but are read out from somewhere else. By setting the argument `includedetails=True` and running the script, it will print which efficiencies are unable to be found. It generates the aforementiones yaml files.
- `yieldplot.py`
  Generates the plots of Figure 11 by reading the aforementioned yaml files and plotting the stated yield with respect to signal values.

B.2 Efficiencies

The efficiencies are calculated by

`/ewprlambda/efficiencies/getRoughEff.py`

which gives a rough estimation of the efficiency. By specifying the ana mode (MM or EE) and the MC sample to run, it calculates the efficiency by taking the number of entries in the MVA tuple of that sample for each q^2, year, track type (LL or DD) and magnet polarity (MD or MU) and divides it by the number of entries in the GenCorct Tuple (or GenGng if GenCorct is not available). This number is multiplied with the GenLvl efficiencies, found in:

`/ewprlambda/tupleproduction/genLevelEffs`

After this script is run for a given MC sample, `mergeEffByLumi.py` is used (with `--tag=rough`) to merge these rough efficiencies according to their luminosity each run. These are the efficiencies that are read out by `YieldEstimations.py` to calculate the expected yields.

C Background yields

The tables are ordered from most abundant background to least abundant background.

C.1 R1

$\Lambda_b^0 \to \Lambda^0 \mu^+ \mu^-$ (muon mode)					
Background	$\mathcal{B}$(bkg)/$\mathcal{B}$(sig)	LL		DD	
		$\epsilon_{\text{bkg}}/\epsilon_{\text{sig}}$	$N_{\text{bkg}}/N_{\text{sig}}$	$\epsilon_{\text{bkg}}/\epsilon_{\text{sig}}$	$N_{\text{bkg}}/N_{\text{sig}}$
$\Lambda_b^0 \to \Lambda_c^+(\to \Lambda^0 \mu^+ \nu_\mu)\mu^- \overline{\nu}_\mu$	$(2.0 \pm 0.7) \times 10^3$	(0.4±0.2%)	7.2 ± 4.2	(0.5±0.2%)	9.9 ± 5.0
$B^0 \to K_S^0(\to \pi^+\pi^-)\mu^+\mu^-$	(63 ± 18)%	No MC available			
$\Xi_b^0 \to \Xi^0(\to \Lambda^0\pi^0)\mu^+\mu^-$	(9.0 ± 4.8)%	No MC available			
$\Xi_b^- \to \Xi^-(\to \Lambda^0\pi^-)\mu^+\mu^-$	(9.3 ± 5.1)%	(0.5±0.2)%	~ 0.1%	(4.0±0.4)%	(0.4±0.2)%
$\Lambda_b^0 \to \Lambda(1520)(\to \Sigma^0(\to \Lambda^0\gamma)\pi^0)\mu^+\mu^-$	(2.6 ± 0.7)%	(5.6±0.8)%	~ 0.1%	(4.5±0.6)%	~ 0.1 %
$\Lambda_b^0 \to \Lambda^0 \psi(2S)(\to \mu^+\mu^-)$	1.0 ± 0.3	~ 0.1%	~ 0.1%	~ 0.1%	~ 0.1%
$\Lambda_b^0 \to \Lambda^0 J/\psi(\to \mu^+\mu^-)$	150 ± 40	$<< 0.1$%	$<< 0.1$%	$<< 0.1$%	$<< 0.1$%

Table 5: Expected amount of background present in the R1 data for the muon mode, estimated using branching fractions (PDG) and efficiencies (MC data). Each entry is a percentage with respect to the amount of signal.

$\Lambda_b^0 \to \Lambda^0 e^+ e^-$ (electron mode)					
Background	$\mathcal{B}$(bkg)/$\mathcal{B}$(sig)	LL		DD	
		$\epsilon_{\text{bkg}}/\epsilon_{\text{sig}}$	$N_{\text{bkg}}/N_{\text{sig}}$	$\epsilon_{\text{bkg}}/\epsilon_{\text{sig}}$	$N_{\text{bkg}}/N_{\text{sig}}$
$\Lambda_b^0 \to \Lambda_c^+(\to \Lambda^0 e^+ \nu_e)e^- \overline{\nu}_e$	$(2.0 \pm 0.7) \times 10^3$	(1.0±0.7)%	19 ± 15	(0.6±0.4)%	12 ± 9.0
$\Lambda_b^0 \to \Lambda^0 \psi(2S)(\to e^+e^-)$	1.0 ± 2.9	(15 ± 3.0)%	(15 ± 5.0)%	(15 ± 2.0)%	(15 ± 5.0)%
$\Lambda_b^0 \to \Lambda^0 J/\psi(\to e^+e^-)$	150 ± 40	(0.2±0.2)%	(3.2±3.4)%	(0.2±0.1)%	(2.2±1.7)%
$B^0 \to K_S^0(\to \pi^+\pi^-)e^+e^-$	(63 ± 18)%	(2.6±0.9)%	(1.6±0.8)%	(4.0±0.9)%	(2.5±0.9)%
$\Xi_b^- \to \Xi^-(\to \Lambda^0\pi^-)e^+e^-$	(9.3 ± 5.1)%	(0.7±0.6)%	~ 0.1%	(9.7±1.6)%	(0.9±0.5)%
$\Lambda_b^0 \to \Lambda(1520)(\to \Sigma^0(\to \Lambda^0\gamma)\pi^0)e^+e^-$	(2.6 ± 0.7)%	(4.2±2.3)%	~ 0.1%	(6.8±2.2)%	~ 0.1%
$\Xi_b^0 \to \Xi^0(\to \Lambda^0\pi^0)e^+e^-$	(9.0 ± 4.8)%	No MC available			

Table 6: Expected amount of background present in the R1 data for the electron mode, estimated using branching fractions (PDG) and efficiencies (MC data). Each entry is a percentage with respect to the amount of signal.

C.2 R2p1

$\Lambda_b^0 \to \Lambda^0 \mu^+ \mu^-$ (muon mode)					
Background	$\mathcal{B}$(bkg)/$\mathcal{B}$(sig)	LL		DD	
		$\epsilon_{\rm bkg}/\epsilon_{\rm sig}$	$N_{\rm bkg}/N_{\rm sig}$	$\epsilon_{\rm bkg}/\epsilon_{\rm sig}$	$N_{\rm bkg}/N_{\rm sig}$
$\Lambda_b^0 \to \Lambda_c^+(\to \Lambda^0 \mu^+ \nu_\mu)\mu^- \overline{\nu}_\mu$	$(2.0 \pm 0.7) \times 10^3$	$(0.5 \pm 0.2)\%$	9.1 ± 4.9	$(0.6 \pm 0.2)\%$	11.2 ± 5.3
$B^0 \to K_S^0(\to \pi^+\pi^-)\mu^+\mu^-$	$(63 \pm 18)\%$	No MC available			
$\Xi_b^0 \to \Xi^0(\to \Lambda^0\pi^0)\mu^+\mu^-$	$(9.0 \pm 4.8)\%$	No MC available			
$\Xi_b^- \to \Xi^-(\to \Lambda^0\pi^-)\mu^+\mu^-$	$(9.3 \pm 5.1)\%$	$(0.5 \pm 0.1)\%$	$\sim 0.1\%$		$(0.3 \pm 0.2)\%$
$\Lambda_b^0 \to \Lambda(1520)(\to \Sigma^0(\to \Lambda^0\gamma)\pi^0)\mu^+\mu^-$	$(2.6 \pm 0.7)\%$	$(5.2 \pm 0.6)\%$	$\sim 0.1\%$	$(4.4 \pm 0.5)\%$	$\sim 0.1\%$
$\Lambda_b^0 \to \Lambda^0 \psi(2S)(\to \mu^+\mu^-)$	1.0 ± 0.3	$\sim 0.1\%$	$\sim 0.1\%$	$\sim 0.1\%$	$\sim 0.1\%$
$\Lambda_b^0 \to \Lambda^0 J/\psi(\to \mu^+\mu^-)$	150 ± 40	$<< 0.1\%$	$<< 0.1\%$	$<< 0.1\%$	$<< 0.1\%$

Table 7: Expected amount of background present in the R2p1 data for the muon mode, estimated using branching fractions (PDG) and efficiencies (MC data). Each entry is a percentage with respect to the amount of signal.

$\Lambda_b^0 \to \Lambda^0 e^+ e^-$ (electron mode)					
Background	$\mathcal{B}$(bkg)/$\mathcal{B}$(sig)	LL		DD	
		$\epsilon_{\rm bkg}/\epsilon_{\rm sig}$	$N_{\rm bkg}/N_{\rm sig}$	$\epsilon_{\rm bkg}/\epsilon_{\rm sig}$	$N_{\rm bkg}/N_{\rm sig}$
$\Lambda_b^0 \to \Lambda_c^+(\to \Lambda^0 e^+ \nu_e)e^- \overline{\nu}_e$	$(2.0 \pm 0.7) \times 10^3$	$(0.7 \pm 0.4)\%$	14 ± 9.2	(1.3 ± 0.4)	25 ± 13
$\Lambda_b^0 \to \Lambda^0 \psi(2S)(\to e^+e^-)$	1.0 ± 2.9	$(17 \pm 1.8)\%$	$(18 \pm 5.3)\%$	$(15 \pm 1.4)\%$	$(15 \pm 4.5)\%$
$\Lambda_b^0 \to \Lambda^0 J/\psi(\to e^+e^-)$	150 ± 40	$<< 0.1\%$	$<< 0.1\%$	$(0.2 \pm 0.2)\%$	$(2.8 \pm 2.6)\%$
$B^0 \to K_S^0(\to \pi^+\pi^-)e^+e^-$	$(63 \pm 18)\%$	No MC available			
$\Xi_b^- \to \Xi^-(\to \Lambda^0\pi^-)e^+e^-$	$(9.3 \pm 5.1)\%$				
$\Lambda_b^0 \to \Lambda(1520)(\to \Sigma^0(\to \Lambda^0\gamma)\pi^0)e^+e^-$	$(2.6 \pm 0.7)\%$	$(0.9 \pm 0.4)\%$	$\sim 0.1\%$	$(8.7 \pm 1.0)\%$	$(0.8 \pm 0.5)\%$
$\Xi_b^0 \to \Xi^0(\to \Lambda^0\pi^0)e^+e^-$	$(9.0 \pm 4.8)\%$	No MC available			

Table 8: Expected amount of background present in the R2p1 data for the electron mode, estimated using branching fractions (PDG) and efficiencies (MC data). Each entry is a percentage with respect to the amount of signal.

C.3 R2p2

$\Lambda_b^0 \to \Lambda^0 \mu^+ \mu^-$ (muon mode)					
Background	$\mathcal{B}$(bkg)/$\mathcal{B}$(sig)	LL		DD	
		$\epsilon_{\text{bkg}}/\epsilon_{\text{sig}}$	$N_{\text{bkg}}/N_{\text{sig}}$	$\epsilon_{\text{bkg}}/\epsilon_{\text{sig}}$	$N_{\text{bkg}}/N_{\text{sig}}$
$\Lambda_b^0 \to \Lambda_c^+(\to \Lambda^0 \mu^+ \nu_\mu)\mu^- \overline{\nu}_\mu$	$(2.0 \pm 0.7) \times 10^3$	$(0.4 \pm 0.1)\%$	8.5 ± 4.0	$(0.4 \pm 0.1)\%$	7.7 ± 3.5
$B^0 \to K_S^0(\to \pi^+\pi^-)\mu^+\mu^-$	$(63 \pm 18)\%$	$(2.3 \pm 0.3)\%$	$(1.4 \pm 0.5)\%$	$(3.0 \pm 0.3)\%$	$(2.0 \pm 0.6)\%$
$\Xi_b^0 \to \Xi^0(\to \Lambda^0\pi^0)\mu^+\mu^-$	$(9.0 \pm 4.8)\%$	$(0.4 \pm 0.1)\%$	$\sim 0.1\%$	$(5.0 \pm 0.2)\%$	$(0.4 \pm 0.2)\%$
$\Xi_b^- \to \Xi^-(\to \Lambda^0\pi^-)\mu^+\mu^-$	$(9.3 \pm 5.1)\%$	$(0.6 \pm 0.1)\%$	$\sim 0.1\%$	$(3.8 \pm 0.2)\%$	$(0.4 \pm 0.2)\%$
$\Lambda_b^0 \to \Lambda(1520)(\to \Sigma^0(\to \Lambda^0\gamma)\pi^0)\mu^+\mu^-$	$(2.6 \pm 0.7)\%$	$(5.3 \pm 0.5)\%$	$\sim 0.1\%$	$(4.3 \pm 0.4)\%$	$\sim 0.1\%$
$\Lambda_b^0 \to \Lambda^0 \psi(2S)(\to \mu^+\mu^-)$	1.0 ± 0.3	$\sim 0.1\%$	$\sim 0.1\%$	$\sim 0.1\%$	$\sim 0.1\%$
$\Lambda_b^0 \to \Lambda^0 J/\psi(\to \mu^+\mu^-)$	150 ± 40	$<< 0.1\%$	$<< 0.1\%$	$<< 0.1\%$	$<< 0.1\%$

Table 9: Expected amount of background present in the R2p2 data for the muon mode, estimated using branching fractions (PDG) and efficiencies (MC data). Each entry is a percentage with respect to the amount of signal.

$\Lambda_b^0 \to \Lambda^0 e^+ e^-$ (electron mode)					
Background	$\mathcal{B}$(bkg)/$\mathcal{B}$(sig)	LL		DD	
		$\epsilon_{\text{bkg}}/\epsilon_{\text{sig}}$	$N_{\text{bkg}}/N_{\text{sig}}$	$\epsilon_{\text{bkg}}/\epsilon_{\text{sig}}$	$N_{\text{bkg}}/N_{\text{sig}}$
$\Lambda_b^0 \to \Lambda_c^+(\to \Lambda^0 e^+ \nu_e)e^- \overline{\nu}_e$	$(2.0 \pm 0.7) \times 10^3$	$(0.4 \pm 0.2)\%$	8.4 ± 5.8	$(0.5 \pm 0.2)\%$	9.3 ± 5.5
$\Lambda_b^0 \to \Lambda^0 \psi(2S)(\to e^+e^-)$	1.0 ± 2.9	$(18 \pm 1.7)\%$	$(18 \pm 5.4)\%$	$(19 \pm 1.4)\%$	$(19 \pm 6.0)\%$
$\Lambda_b^0 \to \Lambda^0 J/\psi(\to e^+e^-)$	150 ± 40	$(0.4 \pm 0.2)\%$	$(5.0 \pm 4.0)\%$	$\sim 0.1\%$	$(2.2 \pm 2.0)\%$
$B^0 \to K_S^0(\to \pi^+\pi^-)e^+e^-$	$(63 \pm 18)\%$	$(3.4 \pm 0.8)\%$	$(2.2 \pm 0.1)\%$	$(2.9 \pm 0.1)\%$	$(1.8 \pm 0.1)\%$
$\Xi_b^- \to \Xi^-(\to \Lambda^0\pi^-)e^+e^-$	$(9.3 \pm 5.1)\%$	$(1.2 \pm 0.4)\%$	$\sim 0.1\%$	$(9.9 \pm 1.0)\%$	$(1.0 \pm 0.5)\%$
$\Lambda_b^0 \to \Lambda(1520)(\to \Sigma^0(\to \Lambda^0\gamma)\pi^0)e^+e^-$	$(2.6 \pm 0.7)\%$	$(6.4 \pm 1.4)\%$	$(0.2 \pm 0.1)\%$	$(4.7 \pm 1.0)\%$	$\sim 0.1\%$
$\Xi_b^0 \to \Xi^0(\to \Lambda^0\pi^0)e^+e^-$	$(9.0 \pm 4.8)\%$	No MC available			

Table 10: Expected amount of background present in the R2p2 data for the electron mode, estimated using branching fractions (PDG) and efficiencies (MC data). Each entry is a percentage with respect to the amount of signal.

D The Λ_c^+ background

This study is located in:

`/ewprlambda/Studies/QsqHigh_backgrounds/LcBackground/`

The `LcBackground.py` script produces the plots shown in this thesis, as well as some additional plots for other categories of the data. In addition, this folder contains some yaml files. These can be used to further estimate the amount of this background present in the data. To do this, a Λ_c^+-veto and an inverse Λ_c^+-veto have to be defined in the RLambda framework. Then the data of the inverse veto can be fit to a combinatorial and signal contribution in the high-q^2 region. The parameters of this fit can be taken and used for a fit to the vetoed data, with an addition of a Λ_c^+-component. Since the main difference between the vetoed region and the inverse vetoed region is this background, the amplitude of this component will be a representation of the amount of this background present in the data.

D.1 MC plots

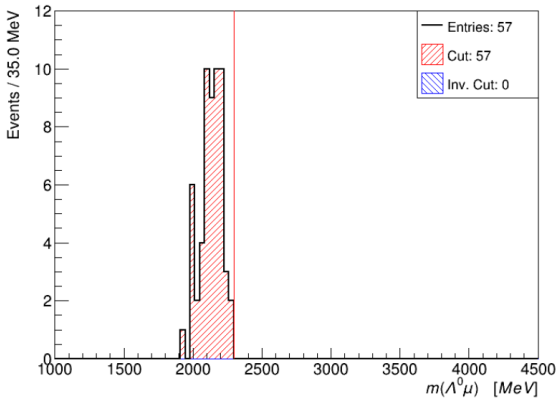

(a) $\Lambda_b^0 \to \Lambda_c^+(\to \Lambda^0\mu^+\nu_\mu)\mu^-\overline{\nu}_\mu$ track DD

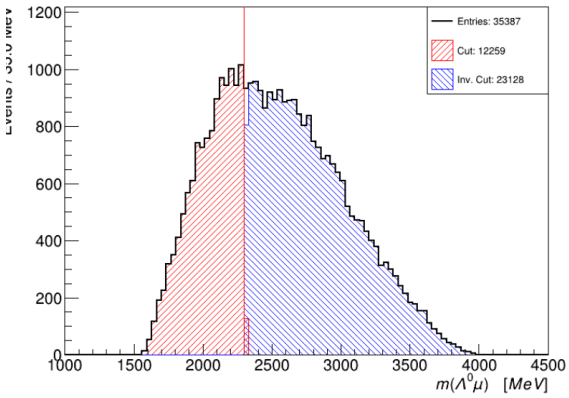

(b) $\Lambda_b^0 \to \Lambda^0\mu^+\mu^-$ track DD

Figure 20: Plots showing the reconstructed $\Lambda^0\mu$ mass, with the MC data separated by the Λ_c^+ mass. The Λ_c^+-veto is applied on the DD MC data of R2p2, after the combinatorial BDT is applied. The LL sample is not shown but is similar.

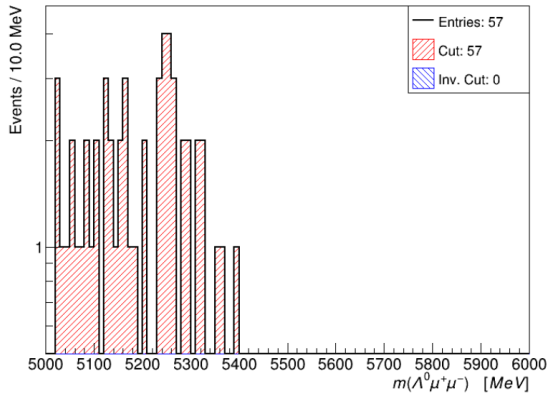

(a) $\Lambda_b^0 \to \Lambda_c^+(\to \Lambda^0\mu^+\nu_\mu)\mu^-\overline{\nu}_\mu$ track DD

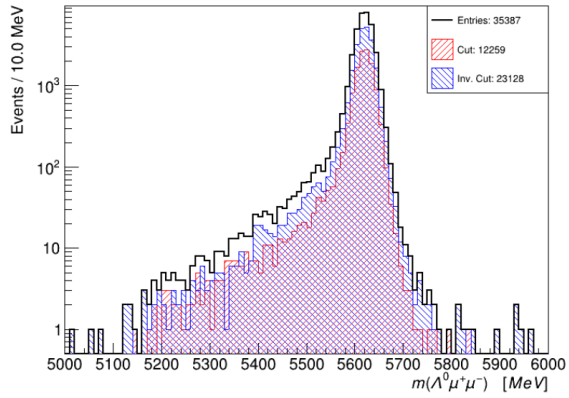

(b) $\Lambda_b^0 \to \Lambda^0\mu^+\mu^-$ track DD

Figure 21: Reconstruction of $m(\Lambda^0\mu^+\mu^-)$ of R2p2 data. The data in red corresponds to the events that have a reconstructed $\Lambda^0\mu$ mass lower than the Λ_c^+ mass and the data in blue have a reconstructed $\Lambda^0\mu$ mass above the Λ_c^+ mass. The LL sample is not shown but is similar.

E $m(\ell^+\nu_\ell)$

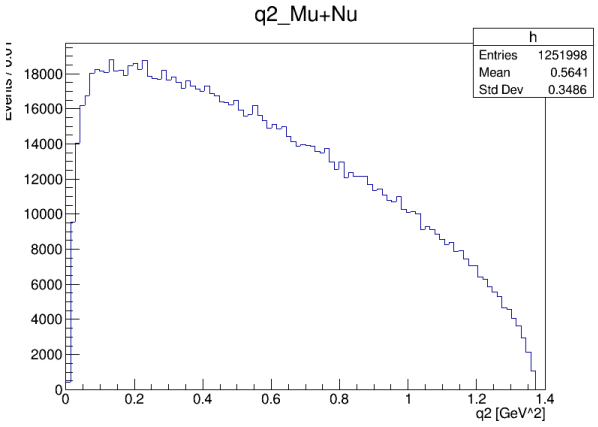

(a) $\Lambda_b^0 \to \Lambda_c^+(\to \Lambda^0\mu^+\nu_\mu)\mu^-\overline{\nu}_\mu$ MC R2p2

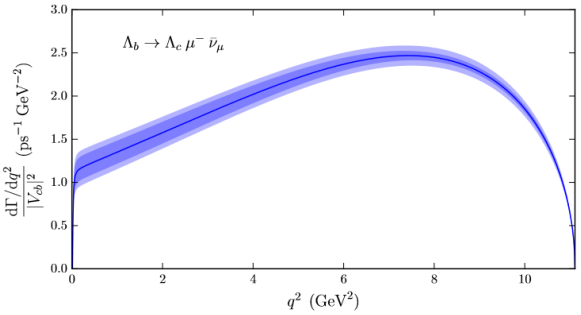

(b) From [29]

Figure 22: $m(\ell^+\nu_\ell)$ distributions from MC $\Lambda_b^0 \to \Lambda_c^+(\to \Lambda^0\ell^+\nu_\ell)\ell^-\overline{\nu}_\ell$ not in agreement with the data as found by [29].

References

[1] Sheldon L. Glashow. "Partial-symmetries of weak interactions". In: *Nuclear Physics* 22.4 (1961), pp. 579–588. ISSN: 0029-5582. DOI: https://doi.org/10.1016/0029-5582(61)90469-2. URL: https://www.sciencedirect.com/science/article/pii/0029558261904692.

[2] Steven Weinberg. "A Model of Leptons". In: *Phys. Rev. Lett.* 19 (21 Nov. 1967), pp. 1264–1266. DOI: 10.1103/PhysRevLett.19.1264. URL: https://link.aps.org/doi/10.1103/PhysRevLett.19.1264.

[3] Abdus Salam. "Weak and electromagnetic interactions". In: *Selected Papers of Abdus Salam*, pp. 244–254. DOI: 10.1142/9789812795915_0034. eprint: https://www.worldscientific.com/doi/pdf/10.1142/9789812795915_0034. URL: https://www.worldscientific.com/doi/abs/10.1142/9789812795915_0034.

[4] Luigi Di Lella and Carlo Rubbia. "The Discovery of the W and Z Particles". In: *Adv. Ser. Direct. High Energy Phys.* 23 (2015), pp. 137–163. DOI: 10.1142/9789814644150_0006.

[5] ATLAS collaboration. "Observation of a new particle in the search for the Standard Model Higgs boson with the ATLAS detector at the LHC". In: *Physics Letters B* 716.1 (Sept. 2012), pp. 1–29. ISSN: 0370-2693. DOI: 10.1016/j.physletb.2012.08.020. URL: http://dx.doi.org/10.1016/j.physletb.2012.08.020.

[6] Andrew G. Cohen, D. B. Kaplan, and A. E. Nelson. "Progress in electroweak baryogenesis". In: *Ann. Rev. Nucl. Part. Sci.* 43 (1993), pp. 27–70. DOI: 10.1146/annurev.ns.43.120193.000331. arXiv: hep-ph/9302210.

[7] Gianfranco Bertone, Dan Hooper, and Joseph Silk. "Particle dark matter: Evidence, candidates and constraints". In: *Phys. Rept.* 405 (2005), pp. 279–390. DOI: 10.1016/j.physrep.2004.08.031. arXiv: hep-ph/0404175.

[8] LHCb collaboration. "Measurement of lepton universality parameters in $B^+ \to K^+\ell^+\ell^-$ and $B^0 \to K^{*0}\ell^+\ell^-$ decays". In: *Phys. Rev. D* 108 (3 Aug. 2023), p. 032002. DOI: 10.1103/PhysRevD.108.032002. URL: https://link.aps.org/doi/10.1103/PhysRevD.108.032002.

[9] Damir Bečirević et al. "Leptoquark model to explain the B-physics anomalies R_K and R_D". In: *Physical Review D* 94.11 (Dec. 2016). ISSN: 2470-0029. DOI: 10.1103/physrevd.94.115021. URL: http://dx.doi.org/10.1103/PhysRevD.94.115021.

[10] Andrzej J. Buras and Jennifer Girrbach. "Left-handed Z' and Z FCNC quark couplings facing new $b \to s\mu^+\mu^-$ data". In: *Journal of High Energy Physics* 2013.12 (Dec. 2013). ISSN: 1029-8479. DOI: 10.1007/jhep12(2013)009. URL: http://dx.doi.org/10.1007/JHEP12(2013)009.

[11] Peter W. Higgs. "Broken Symmetries and the Masses of Gauge Bosons". In: *Phys. Rev. Lett.* 13 (16 Oct. 1964), pp. 508–509. DOI: 10.1103/PhysRevLett.13.508. URL: https://link.aps.org/doi/10.1103/PhysRevLett.13.508.

[12] Wikimedia Commons. *Standard Model of Elementary Particles*. 2019. URL: https://commons.wikimedia.org/wiki/File:Standard_Model_of_Elementary_Particles.svg.

[13] Nicola Cabibbo. "Unitary Symmetry and Leptonic Decays". In: *Phys. Rev. Lett.* 10 (12 June 1963), pp. 531–533. DOI: 10.1103/PhysRevLett.10.531. URL: https://link.aps.org/doi/10.1103/PhysRevLett.10.531.

[14] Makoto Kobayashi and Toshihide Maskawa. "CP-Violation in the Renormalizable Theory of Weak Interaction". In: *Progress of Theoretical Physics* 49.2 (Feb. 1973), pp. 652–657. ISSN: 0033-068X. DOI: 10.1143/PTP.49.652. eprint: https://academic.oup.com/ptp/article-pdf/49/2/652/5257692/49-2-652.pdf. URL: https://doi.org/10.1143/PTP.49.652.

[15] LHCb collaboration. "Test of lepton universality with $\Lambda_b^0 \to pK^-\ell^+\ell^-$ decays". In: *Journal of High Energy Physics* 2020.5 (May 2020). ISSN: 1029-8479. DOI: 10.1007/jhep05(2020)040. URL: http://dx.doi.org/10.1007/JHEP05(2020)040.

[16] LHCb collaboration. "Tests of Lepton Universality Using $B^0 \to K_S^0\ell^+\ell^-$ and $B^+ \to K^{*+}\ell^+\ell^-$ Decays". In: *Phys. Rev. Lett.* 128 (19 May 2022), p. 191802. DOI: 10.1103/PhysRevLett.128.191802. URL: https://link.aps.org/doi/10.1103/PhysRevLett.128.191802.

[17] Scholarpedia. *Summary of lepton flavour universality tests performed using rare b-hadron decays*. 2023. URL: http://www.scholarpedia.org/article/File:Rare-decay-flavour-universality.png.

[18] William Detmold and Stefan Meinel. "$\Lambda_b^0 \to \Lambda^0 \ell^+ \ell^-$ form factors, differential branching fraction, and angular observables from lattice QCD with relativistic b quarks". In: *Physical Review D* 93.7 (Apr. 2016). ISSN: 2470-0029. DOI: 10.1103/physrevd.93.074501. URL: http://dx.doi.org/10.1103/PhysRevD.93.074501.

[19] Thomas Blake, Stefan Meinel, and Danny van Dyk. "Bayesian analysis of $b \to s\mu^+\mu^-$ Wilson coefficients using the full angular distribution of $\Lambda_b \to \Lambda(\to p\pi^-)\mu^+\mu^-$ decays". In: *Phys. Rev. D* 101 (3 Feb. 2020), p. 035023. DOI: 10.1103/PhysRevD.101.035023. URL: https://link.aps.org/doi/10.1103/PhysRevD.101.035023.

[20] "LHCb detector performance". In: *International Journal of Modern Physics A* 30.07 (Mar. 2015), p. 1530022. ISSN: 1793-656X. DOI: 10.1142/s0217751x15300227. URL: http://dx.doi.org/10.1142/S0217751X15300227.

[21] LHCb collaboration. "Measurement of the track reconstruction efficiency at LHCb". In: *Journal of Instrumentation* 10.02 (Feb. 2015), P02007. DOI: 10.1088/1748-0221/10/02/P02007. URL: https://dx.doi.org/10.1088/1748-0221/10/02/P02007.

[22] LHCb collaboration. "Performance of the LHCb RICH detector at the LHC". In: *The European Physical Journal C* 73.5 (May 2013). ISSN: 1434-6052. DOI: 10.1140/epjc/s10052-013-2431-9. URL: http://dx.doi.org/10.1140/epjc/s10052-013-2431-9.

[23] Roel Aaij et al. "Design and performance of the LHCb trigger and full real-time reconstruction in Run 2 of the LHC". In: *JINST* 14.04 (2019), P04013. DOI: 10.1088/1748-0221/14/04/P04013. arXiv: 1812.10790 [hep-ex].

[24] LHCb Starterkit. *LHCb Dataflow*. 2020. URL: https://lhcb.github.io/starterkit-lessons/first-analysis-steps/dataflow.html.

[25] LHCb collaboration. "Differential branching fraction and angular analysis of $\Lambda_b^0 \to \Lambda\mu^+\mu^-$ decays". In: *JHEP* 06 (2015). [Erratum: JHEP 09, 145 (2018)], p. 115. DOI: 10.1007/JHEP06(2015)115. arXiv: 1503.07138 [hep-ex].

[26] William Detmold and Stefan Meinel. "$\Lambda_b \to \Lambda\ell^+\ell^-$ form factors, differential branching fraction, and angular observables from lattice QCD with relativistic b quarks". In: *Phys. Rev. D* 93 (7 Apr. 2016), p. 074501. DOI: 10.1103/PhysRevD.93.074501. URL: https://link.aps.org/doi/10.1103/PhysRevD.93.074501.

[27] Lex Marinus Greeven. "Decoding beauty: rare baryonic decays SciFi detector commissioning". PhD thesis. Maastricht University, 2024. ISBN: 9789464960563. DOI: 10.26481/dis.20240403lg.

[28] R. L. Workman et al. "Review of Particle Physics". In: *PTEP* 2022 (2022), p. 083C01. DOI: 10.1093/ptep/ptac097.

[29] William Detmold, Christoph Lehner, and Stefan Meinel. "$\Lambda_b \to p\ell^-\overline{\nu}_\ell$ and $\Lambda_b \to \Lambda_c\ell^-\overline{\nu}_\ell$ form factors from lattice QCD with relativistic heavy quarks". In: *Physical Review D* 92.3 (Aug. 2015). ISSN: 1550-2368. DOI: 10.1103/physrevd.92.034503. URL: http://dx.doi.org/10.1103/PhysRevD.92.034503.